Algorithmic determination of measurement locations for surface point markers in sheet metal forming and application in inverse modelling – A numerical and experimental study

Journal Article

Author(s):
Ryser, Matthias ⓘD; Hora, Pavel; Bambach, Markus ⓘD

Algorithmic determination of measurement locations for surface point markers in sheet metal forming and application in inverse modelling – A numerical and experimental study

Matthias Ryser [a,b,*], Pavel Hora [b], Markus Bambach [a,b]

[a] *Advanced Manufacturing Laboratory, ETH Zurich, 8005 Zurich, Switzerland*
[b] *Institute of Virtual Manufacturing, ETH Zurich, 8005 Zurich, Switzerland*

A B S T R A C T

A key requirement for the use of smart process and quality control systems in sheet metal forming is the ability to determine representative observables as well as their measurement locations. The observable used most often in deep drawing is the movement of the sheet border, which is referred to as draw-in. Due to the usually large distance between the sheet border and the areas of the largest plastic deformation, literature provides indications that more representative locations for the characterization of the material flow exist. In this work, a novel algorithmic method is proposed that allows to determine the optimal locations at which the material flow should be measured. The method is applied on surface markers on a cup, whose displacement is measured ex situ using a stripe projection scanner. The indications in the literature are confirmed, with the most sensitive markers found in, or directly above the die radius in the side wall of the cup, where an increase in the sensitivity of the marker displacement by 51% compared to the draw-in is observed. A comparison of markers positioned at different radii on the initial sheet reveals a clear correlation between the sensitivity of the markers and the predictive accuracy if their displacement is used as observable to predict the sheet thickness and process parameters in an inverse manner. This highlights the importance of new methods for the selection of measurement positions. This work therefore aims at contributing to novel inline quality observation concepts in sheet metal forming.

1. Introduction

Deep drawing is one of the most often used manufacturing processes for processing sheet metals. This is particularly true for the automotive industry, where almost all car body parts are produced by deep drawing. In the process, the sheet metal blank is clamped in a blank holder and a die and drawn over a punch. Geometrical properties of punch and die as well as the blank holder are then mapped into the sheet. Well-structured and more detailed information about the process and its mechanics is provided for example by Tschaetsch (2006).

To increase the robustness of the process, many efforts have been made to integrate smart data-driven process control systems into the real industrial process. Lim et al. (2008) provide a comprehensive review about developments towards control in deep drawing made until 2008. In their work, the authors review the different actuator and sensor concepts provided by literature and state in their conclusion that besides the determination of reference trajectories and accurate models for the

controller, the key technical challenge consists of the development of cost-effective and reliable sensor concepts to measure representative process variables. The work provided by Polyblank et al. (2014), which builds on the review of Lim et al. (2008) and others, deals not only with closed-loop control in deep drawing, but with material forming in general. Their work aims at identifying research gaps for future developments in closed-loop control in metal forming, like dynamic trajectories which are determined using simulation models (Table 8 in (Polyblank et al., 2014)) as a specific example related to deep drawing. Furthermore, the authors conclude that one key feature for future control systems is the usage of faster predictive models to detect scrap parts before they occur, which again highlights the importance of the determination of representative observables. The most inclusive review was written by Allwood et al. (2016) in CIRP Annals – Manufacturing Technology in 2016, where the authors analyse future potentials for closed-loop control in material forming, as similarly done by Polyblank et al. (2014). Considering again the conclusion with respect to deep

---

drawing, the authors identify great potential for new sensor concepts for the spatial characterization of the final workpiece to improve closed-loop control concepts. Despite all the efforts put into smart process control, no particular control system has been established. A brief history over the most important approaches proposed in the literature shall be given in the following.

Observation and control of part quality requires the definition and measurement of observables. These can either be measured before or during and after the forming process. Mainly focussing on the first category is the work provided by Heingärtner (2012). By using the eddy current principle to estimate material properties directly in the production line *before* the part is manufactured, Heingärtner (2012) managed to infer yield strength, tensile strength, and uniform elongation and Lankford parameters. The method proposed provides a possibility to determine material properties in a non-destructive way directly in the production line and feed that information back for the use in process control. Mork (2012) used these type of material properties to predict quality criteria like local wrinkling or local thinning by using neural networks. The author concludes that these predictions are suitable for process control in combination with spacing blocks between blank holder and die as actuators. As a drawback, the process adjustments are only made as a function of the material properties and therefore other disturbances, like temperature changes, are not taken into account. In contrast to this pre-process measurements of material properties, most other approaches found in the literature focus on the measurement of distance-based observables during the forming process.

The distance-based observable most often used in deep drawing is the draw-in of the sheet border. Wang et al. (2005) investigated the use of the global draw-in as observable to assess the quality of deep drawing tools after tool try-out. The authors describe the draw-in as the single most important stamping index which is directly correlated to all other forming characteristics. The draw-in has therefore been used extensively as observable for process control. Building on this knowledge, Neugebauer et al. (2006) investigated a new concept for process control in deep drawing in close collaboration with the automotive industry. In their work, the authors used the draw-in as observable and piezo actuators to increase or decrease the blank holder pressure locally. Endelt et al. (2013) are going one step further and propose a closed-loop control system controlling the material flow *during* the press stroke using the draw-in as observable. The authors specifically note in the conclusion that it is possible to control the material flow using only the draw-in as observable in their case and provide more detail about the experimental setup in the publication by Tommerup and Endelt (2012). Note that since there are so many references about the use of flange draw-in measurements, this is a non-exhaustive list. A novel concept has recently been proposed by Baral et al. (2022). In their work, the authors equipped a Marciniak-type punch with three acoustic emission sensors. By using triangulation of the sensor signals and evaluating the time difference of the arriving signals to each sensor, the authors were able to predict not only the onset of necking, but also the location of necking and fracture accurately. The above mentioned review by Allwood et al. (2016) provides a comprehensive and well-structured overview over many different approaches provided by literature.

In contrast to measuring the material flow only at the sheet border, Griesbach (2000) investigated different methods for the global characterization of the material flow in deep drawing. The author arrives at the conclusion that the material flow should be characterized in the areas of the part where the largest plastic deformation occurs during forming and not only at the sheet border (see (Griesbach, 2000) on page 29, 32 and 33). Considering a simple cup-drawing process and since the forming area is in this case mainly located in the part flange in the form of radial tension and tangential compression, the author proposes to measure the material flow at the sheet border and additionally at the beginning and end of the die radius. The author uses two different measurement methods, one being an optical sensor measuring the passing of a marking on the sheet and the other being a roller ball sensor similar to computer

mouses in the old days as described by Doege et al. (2002). Following the same reasoning, Maier et al. (2017) proposed to measure the length of the skid-lines as observable which are caused by the first contact between the sheet and tool radii in combination with the relative movement of the sheet. Although the authors of both references argue that the material flow measurement in the immediate vicinity of the main forming zone contains a larger sensitivity towards perturbations in the process parameters, this hypothesis is not proven in either of the two references in a quantitative way. To the best knowledge of the authors, these two references are the only ones who provide a specific location for the measurement of the material flow.

For all of the previously mentioned observables, the determination of measurement locations is required. In order to determine suitable locations for draw-in measurements, Harsch et al. (2017) used stochastic finite element simulations to determine the correlation coefficients between many different measurement locations around the part and all quality criteria like sheet thinning and risk of wrinkles. The authors then selected manually multiple locations with a high correlation coefficient. Since correlations between the selected sensor positions are not taken into account, this approach may lead to an excessive number of sensors. Neuhauser et al. (2019) therefore identified optimal sensor positions by selecting the most independent columns in the sensitivity matrix containing the sensitivity of each sensor position (columns) on each quality criteria (rows). The method proposed by Neuhauser et al. (2019) is a promising approach since it allows the algorithmic determination of sensor positions in contrast to all other previously existing approaches in which the measurement positions are selected manually. Since the sensitivities were determined by the slope of a regression model with linear features, this approach is limited to only linear surrogate models. Finally, Kott et al. (2021) identified sensor positions by using backward selection, in which first all sensor positions are selected and in an iterative procedure, the one which leads to the least drop in accuracy if neglected is eliminated. Note that depending on the amount of sensor positions considered, this procedure leads to a tremendous computing time due to its exponential dependence on the number of features considered at the beginning.

In previous work by the authors Ryser et al. (2021), the approach proposed by Neuhauser et al. (2019) was extended by using nonlinear sensitivity metrics to model process parameters dependent on draw-ins and local blank holder forces. The study was done on a side panel frame, and 20 out of 21 process and material parameters were inversely determined with a coefficient of determination equal to 0.9 or higher on the test set. Nonlinear sensitivity metrics allow the use of nonlinear surrogate models for the sensitivity analysis like higher order regression or neural networks, which first might lead to a higher modelling accuracy for surrogate modelling and second allow the consideration of geometrically highly nonlinear sensor signals like the displacement of material points in 3D space.

Although being a very fundamental problem, the current state of the art provides no *quantitative* and systematic analysis about how the most sensitive areas of the material flow can be identified. On the one hand, literature provides only qualitative investigations about areas of higher and lower sensitivity which are based on theoretical elasto-plastic considerations as outlined above. On the other hand, first approaches have been proposed to systematically determine measurement locations for the draw-in as opposed to the global material flow, which is considered to be a less difficult problem since the draw-in is usually described as a one-dimensional quantity. First, the authors hypothesize that by generalizing the models and methods proposed by Ryser et al. (2021) such that they can be applied on material points at any location instead of just the edge of the sheet metal, it is possible to determine qualitatively and quantitatively which areas on the sheet are most sensitive. It is then assumed that evaluating these sensitivities allows to investigate whether the hypothesis of improved predictive performance by generalizing the concept of the draw-in made by Griesbach (2000) and Maier et al. (2017) is supported or not. Second, the authors hypothesize that if

a discrete set of sensitive material flow measurement locations can be identified, it is possible to establish models that allow the inverse identification of the process input and quantitative estimation of quality criteria based on the measured material flow at predefined locations on the sheet. These models are then validated using first, simulations and second, experimental data.

Note that the term *inverse approach* is in the literature mostly used in a fundamentally different context compared to this work. Guo et al. (2000) describe in their review the *inverse approach* as a simplified simulation approach, in which the final shape of the desired part is known and the local deformations are estimated by comparison with the initial blank. Using simplified descriptions of the constitutive equations and tool actions, manufacturability of the part can thus be evaluated. In this paper, the authors refer to inverse models as models that directly map from measured output quantities like the material flow measurements to the initial process parameters as well as quality criteria like local thinning by using a functional relationship.

This manuscript is organized as follows. Section 2 contains all relevant material parameters and experimental methods. Section 3 explains the computational workflow, whose simulative and experimental results are then documented in Section 4. The results are interpreted in Section 5, and final conclusions are drawn in Section 6.

2. Material and experimental methods

2.1. Material used: Aluminium AA6014-T4

The sheet material used in this work is the aluminium alloy AA6014-T4 which is a standard material used for structural and outer skin parts in the automotive industry according to Ostermann (2014) (page 524). Its chemical composition is given in Table 1. For the use in the FEM-simulation, hardening curve, yield locus and forming limit curve (FLC) were characterized. Since the design of experiments (DoE) in this work contains only experiments without failure, the determined FLC is technically irrelevant for this work. For the sake of completeness, it is still included here as a reference for the research audience as well as for future work.

For the characterization of the flow behaviour in uniaxial stress state, tensile tests were performed in 45° intervals from rolling direction (RD) to transversal direction (TD) using three repetitions per configuration and evaluated according to DIN EN ISO 6892–1 (2020) and DIN EN ISO 10113 (2021). The Young's modulus was determined as $E = 75048 MPa$ in the technical strain interval [0, 0.0015]. Since the force maximum occurs at an equivalent plastic strain of $\varepsilon_{eq} \approx 0.175$ but the maximum equivalent strains reached during cup-drawing were $\varepsilon_{eq} \approx 0.5$, the plastic stress-strain curve from the tensile test in RD was elongated using the one obtained in the bulge test. The bulge test was performed and evaluated according to DIN EN ISO 16808 (2021). Best fitting results of the flow stress were obtained by using the Hockett-Sherby approximation proposed by Hockett and Sherby (1975) given by Eq. (1), which is in accordance with literature provided by Hippke et al. (2020) and Herrmann (2020). Premature failure in the simulation due to insufficient hardening for strains beyond uniform elongation was observed which is most probably caused by the convergence of the flow stress towards the parameter A in the Hockett-Sherby-approach. Similarly, Pham and Kim (2022) investigated the flow behaviour of six different aluminium alloys and steels and concluded that a saturation law or power law alone might lead to poor performance for the prediction of the flow stress for large strain ranges. Taking into account this result, a flow curve was

superimposed using the formulation according to Swift (1952) given by Eq. (2) using a mixed formulation given by Eq. (3), similarly done by Chen et al. (2019) and Harsch et al. (2017) for the same aluminium alloy. The experimentally obtained plastic stress-strain relationship as well as the fitted flow curve are visualized in Fig. 1 and the corresponding flow curve parameters are given in Table 2. As can be seen in Fig. 1, the slope of the hardening curve of the approximation is in good accordance with the experiments, including its slope for higher strains with the additional part according to Swift.

$$\sigma_{HS} = A - (A - B)\cdot\exp(-m\varepsilon_{eq}{}^p) \tag{1}$$

$$\sigma_{Swift} = C(D + \varepsilon_{eq})^n \tag{2}$$

$$\sigma_{comb} = \alpha\cdot\sigma_{Swift} + (1 - \alpha)\cdot\sigma_{HS} \tag{3}$$

As yield locus, YLD2000 was used in the 2D formulation, considering only in-plane stresses and isotropic hardening according to Barlat et al. (2003). This formulation is also used by Hippke et al. (2020), Herrmann (2020) and Harsch et al. (2017) for the same material. To fit the yield locus, R-values and $R_{p0.2}$ in all three directions as well as the biaxial R-value R_b and biaxial yield stress σ_b were used. To comply with recent developments in the literature which propose the inverse calibration of the flow exponent M with an additional experiment in the plane strain state, notched tensile tests were performed and the exponent M was fitted with the procedure proposed by Hippke et al. (2020), leading to a value of $M = 5.813$ (average of three repetitions). This result is consistent with the one obtained by Hippke et al. (2020) where $M = 5.89$ was determined for the same material. The experimental results used for the fit of the yield locus are given in Table 3 and the finally obtained yield locus is visualized in Fig. 2.

To determine the forming limit curve (FLC), seven different specimen geometries with widths of $20, 50, 80, 90, 100, 120$ and $200 mm$ as well as a length of $200 mm$ were drawn over a hemispherical punch with
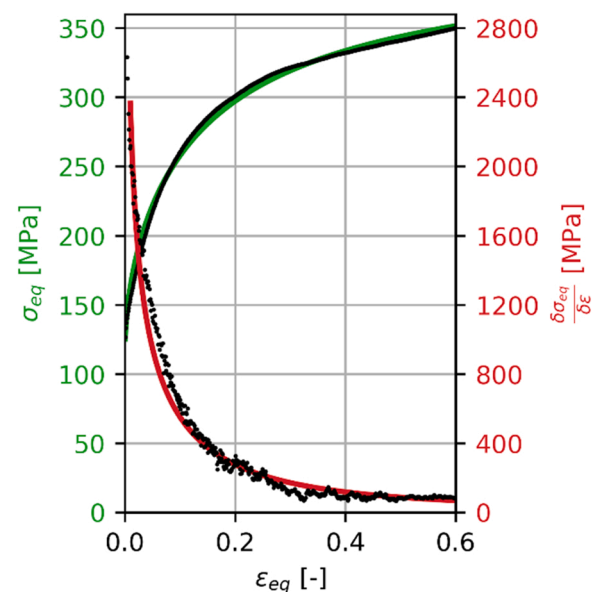

Fig. 1. Hardening curve (green: approximation, black: experimental) and its slope (red: approximation, black: experimental) for the aluminium alloy AA6014-T4.

Table 1
Chemical composition (wt%) of the aluminium AA6014-T4 used, based on the material data sheet of the material supplier.

Cr	Si	Fe	Cu	Mn	Mg	Zn	Ti	V	Others, each	Others, total
0.20	0.30–0.60	0.35	0.25	0.05–0.20	0.40–0.80	0.10	0.10	0.05–0.20	0.05	0.15

Table 2

Flow curve parameters determined for the combined Swift – Hockett-Sherby approach for the aluminium alloy AA6014-T4.

A[MPa]	B[MPa]	p[-]	m[-]	C[MPa]	D[-]	n[-]	α[-]
356.30	114.46	0.812	6.12	397	0.005	0.194	0.40

a diameter of 100*mm*. The displacement of the part flange was fully suppressed by using lock beads. Each configuration was performed three times and evaluated using the cross-section method according to DIN EN ISO 12004–2 (2021), leading to a slightly more conservative FLC compared to the time-dependent method according to Volk and Hora (2011). Thus, the former one was used. The obtained forming limit curve is visualized in Fig. 3.

2.2. Experimental design of the cup-drawing used in this study

As a case study, the well-known cup-drawing process was used which has the positive side effect that the results are intuitively interpretable due to the low geometrical complexity and that large virtual as well as experimental data set can be created with minimum efforts due to the simple process setup. The final cup geometry is visualized in Fig. 4. The parts were drawn on a double action press from Walter+Bai RK-A60SF with adjustable blank holder force of up to 300*kN* which is visualized in Fig. 5(a). The lubricant used was Molykote EM-30 L. The initial blanks are circular shaped with a diameter of 190*mm* and a thickness of 1.15*mm*. Based on the initial diameter of the sheet and the punch, a drawing ratio of $\beta = 1.92$ results. This value is close to the maximum achievable drawing ratio, which was determined for example by Herrmann and Merklein (2018) (see Fig. 4 in the reference) as $\beta_{max} = 2.05$ for the same material. It has to be noted that β_{max} cannot be used in this case, since any variation in the process parameters would lead to immediate failure. The drawing ratio was chosen large in order to maximize the signal to noise ratio in the measurement values.

The blank holder force and the initial sheet position in X and Y direction were used as independent parameters of the process to alternate the restraining conditions acting on the blank. Whereas the blank holder force can be adjusted on the machine continuously, the initial sheet position is set by templates whose inner hole diameter matches the outer diameter of the initial blank. The templates have a thickness of 1*mm* which is lower than the one of the sheet. The template can therefore remain inserted in the machine when the blank holder is closed, providing a geometrically defined position of the sheet during closing of the blank holder. The inserted template is highlighted in Fig. 5(a) and the nine templates used are visualized qualitatively in Fig. 5(b).

The upper limits for each parameter in the DoE were chosen as large as possible, but such that no failure occurs. The minimum blank holder force was set to 80*kN* since wrinkling occurs for lower values, and the initial position of the blank was only alternated in positive X and Y direction due to symmetry. The parameter space for the initial position was divided into three equally spaced levels to cover the whole range. In the experiment, a very small sensitivity of the blank holder force on the material flow was observed, hence the third level besides minimum and maximum value was neglected, since no further insight was expected. To span the parameter space, a full factorial DoE was used, which is visualized in Fig. 6. The levels selected in the DoE are equal to the axis labels in Fig. 6, leading to 18 combinations in total.

2.3. Measurement of material flow and sheet thickness

The 3D stripe projection scanner GOM ATOS core 135 was used to digitize the deep drawn cups. In contrast to in situ measurements which are mostly carried out in the literature, this ex situ measurement device was used for the characterization of the material flow which allows the tool design to be completely independent of the measurement device in real use. As a drawback, this measurement method does not allow to determine the material flow over time. However, a significant gain of insight by in situ measurements of the material flow is not expected in this case, as the process parameters are chosen statically.

After the digitization of the cup, a 3D frame of reference (FoR) was defined dependent on geometrical features of the cup. First, a virtual plane was fitted on the upper side of the flange to block the rotational
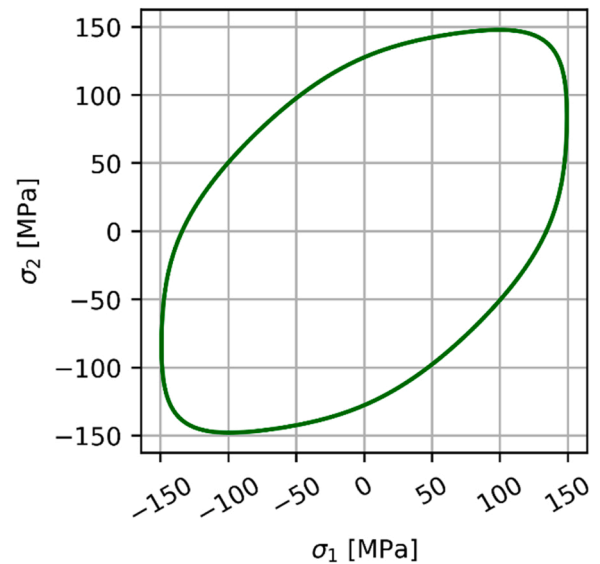

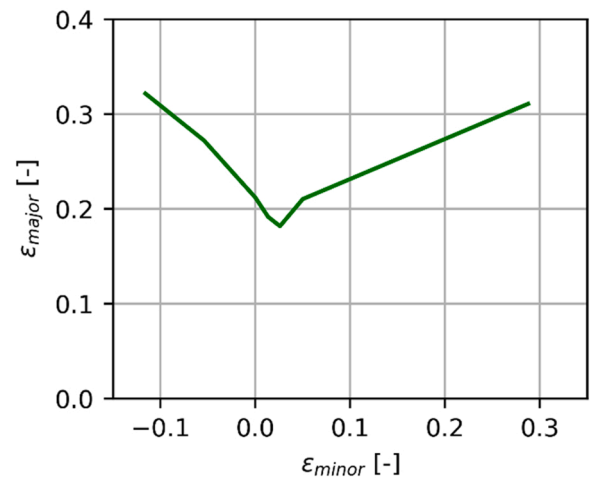**Fig. 2.** Yield locus using YLD2000 formulation obtained for the aluminium alloy AA6014-T4.

Fig. 3. FLC obtained using the cross section-method based on DIN 12004–2 for the aluminium alloy AA6014-T4.
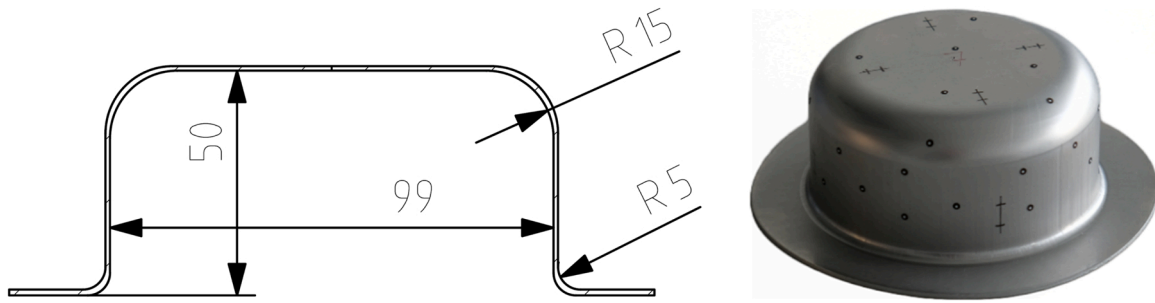
Table 3

Parameters used for the yield locus YLD2000 for the aluminium alloy AA6014-T4.

σ_o[MPa]	σ_{45}[MPa]	σ_{90}[MPa]	σ_b[MPa]	R_0[-]	R_{45}[-]	R_{90}[-]	R_b[-]	M[-]
134.15	130.63	127.68	136.52	0.846	0.516	0.746	0.979	5.813

Fig. 4. Geometrical features of the cup geometry (left) and experimentally obtained cup (right) used in this work.

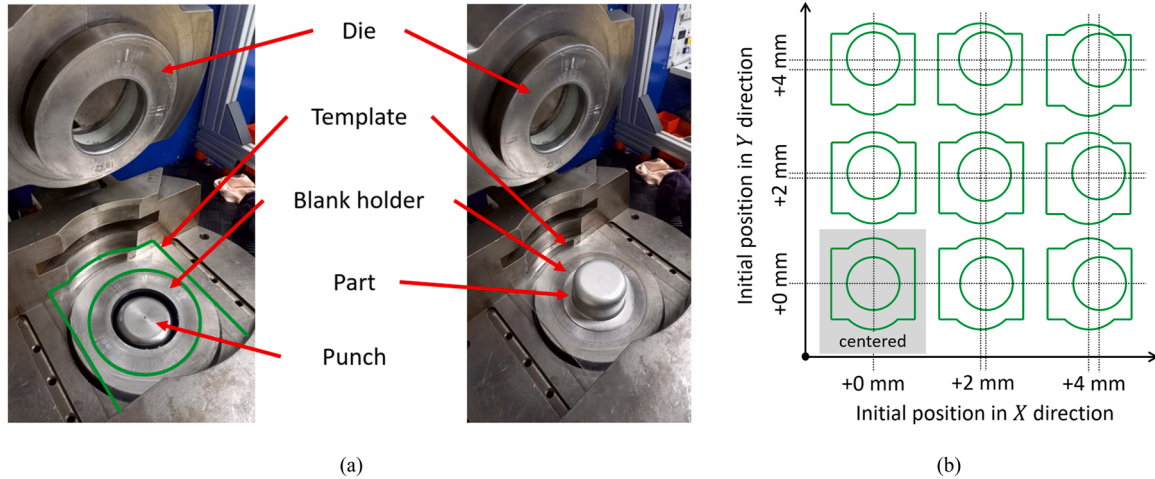(a)   (b)

Fig. 5. Press machine used for cup-drawing consisting of the three main tools punch, blank holder and die. On the right, the nine templates used for blank positioning are visualized. The templates contain a lower material thickness compared to the sheet and thus can remain inserted throughout processing due to the increase of the material thickness of the sheet in the flange area. Note that the movement of the initial position in (b) is exaggerated for illustrative purposes.
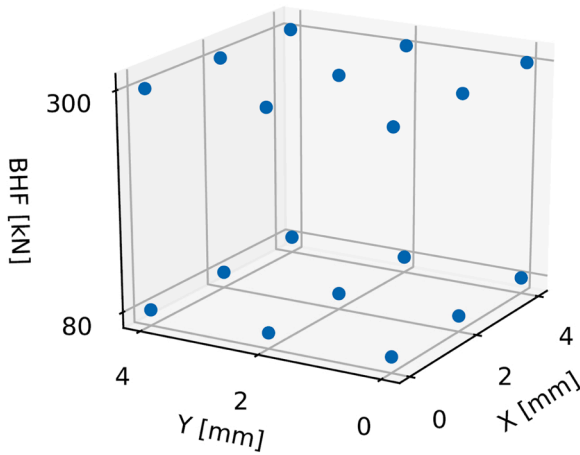

Fig. 6. Experimental DoE used for model validation in this work (BHF = blank holder force, X = initial X position of the sheet, Y = initial Y position of the sheet). Grid lines match the parameter sets used in the DoE.

degrees of freedom (DoF) around the X and Y axes and the translational DoF in Z direction. Second, a cylinder was fitted on the outside of the side wall whose central axis was intersected with the plane from step 1. This yields the origin of the coordinate system and thereby blocks the translational DoF in X and Y direction. To block the remaining rotational DoF around the central axis, the positive X direction was defined by a mark on the sheet in rolling direction. To determine the drawing depth of each cup, a second virtual plane was fitted on the upper side of the top

surface and intersected with the central axis of the cylinder. The distance between this point and the origin therefore corresponds to the drawing depth. For the fitting of the planes and the cylinder mentioned, the corresponding digitized surfaces were first selected using the geometry-based selection function in GOM Professional, and the elements fitted using the Gaussian best-fit method considering all surface points located within $\pm 3\sigma$ around the mean surface, which effectively results in a least squares fit of the geometrical elements to the measured surface. Fig. 7(a) shows a digitized cup and Fig. 7(b) visualizes the previously mentioned geometrical features for the determination of the frame of reference. After alignment of the part according to the coordinate system, the markings drawn on the initial sheet were visible on the scanned part due to the contrast between dark (marking) and light (sheet), and were then manually read out in the GOM software by defining surface points in the middle of the mark. The material flow at these points was then determined by the difference between final and initial position of marked points on the sheet as illustrated in Fig. 7(c) as green lines. For the thickness measurements, the drawn cups where cut into four quarters by wire erosion and the wall thickness was measured with the microscope Keyence VHX-7000 as exemplified in Fig. 7(d). The locations of the thickness measurements are visualized below in Fig. 9 as green boxes, in which the thickness was evaluated in the centre point for each box.

2.4. Simulation setup of cup-drawing

All simulations were performed with the AutoForm R8-solver using the material model given in Section 2.1. The tools were modelled as rigid bodies with the tool geometry derived from the part illustrated in Fig. 4 and a drawing gap of $1.45mm$, as on the real tool, between punch and
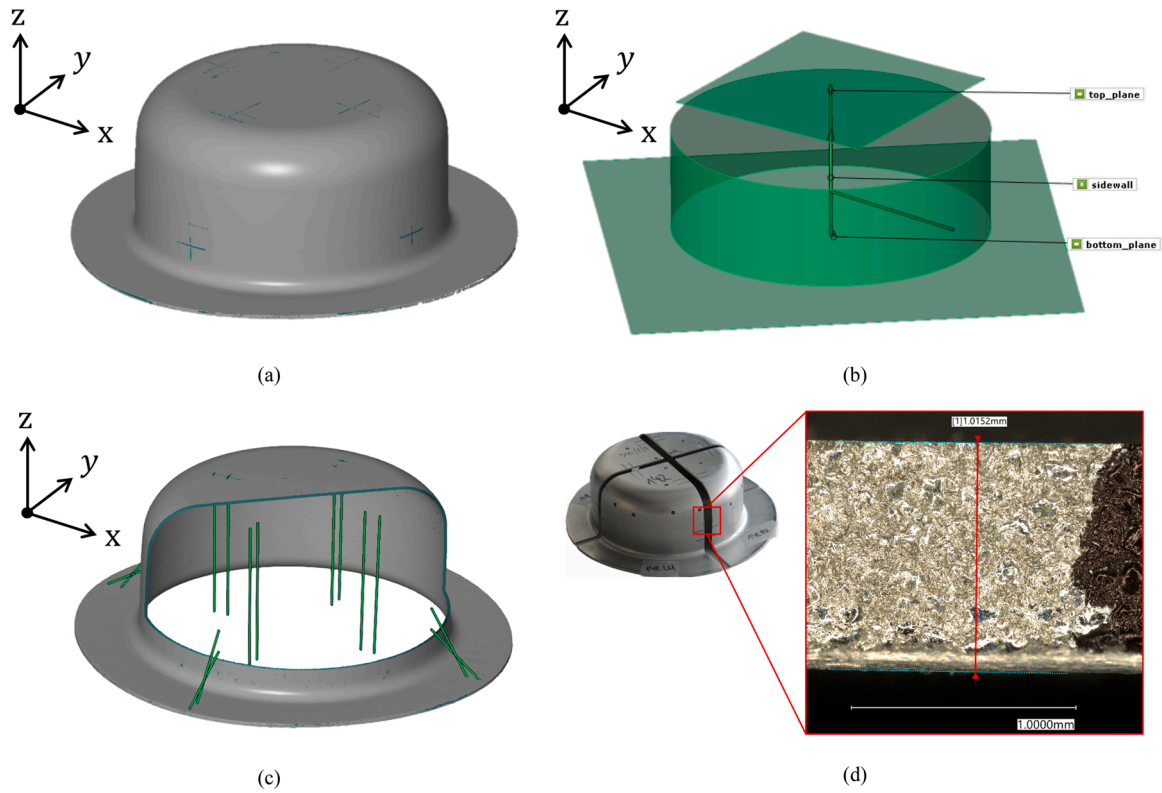
Fig. 7. (a) Digitized cup with GOM ATOS, (b) fitting elements used for the definition of the frame of reference, (c) visualization of surface point marker displacement for 16 SPMs visualized in green, (d) visualization of thickness measurement.

die. A too high sensitivity of the blank holder force on the draw-in was observed with a constant friction coefficient caused by a too high restraining force for high values of the blank holder pressure. To overcome this issue, the pressure dependent friction law available in Auto-Form and given by Eq. (4) was used, with p being local pressure. The importance of considering the pressure-dependence of the friction coefficient was also observed by Zöller et al. (2015). In their work, Zöller et al. (2015) compared the friction model with a constant coefficient according to Coulomb with a modified version considering pressure dependence given by Eq. (4). The authors observed a significantly better agreement between experiment and simulation w. r. t. sheet thickness and punch force if pressure dependence was included, especially for the case of alternating blank holder forces as is the case in the work provided here.

$$\mu = \mu_0 \left(\frac{p}{p_0} \right)^{\varepsilon - 1} \tag{4}$$

In Eq. (4), μ_0, p_0 and ε are model parameters. The drawing experiments were performed at a low punch velocity of $1mm/s$ and thus the velocity dependence can effectively be neglected. Note that due to its mathematical form, Eq. (4) contains only two degrees of freedom since

$$\mu = \mu_0 \left(\frac{p}{p_0} \right)^{\varepsilon - 1} = \frac{\mu_0}{(p_0)^{\varepsilon - 1}} p^{\varepsilon - 1} = const \cdot p^{\varepsilon - 1} \tag{5}$$

The dependent model parameter p_0 was chosen as $p_0 = 1MPa$. The remaining two independent parameters μ_0 and ε were identified by minimizing the sum of the squared error of the draw-in in $0°$, $90°$, $180°$ and $270°$ to RD for a blank holder force of $80kN$ and $300kN$ between experiment and simulation. The resulting model parameters are given in Table 4. The values obtained are in a similar range compared to the ones obtained by Zöller et al. (2015).

For spatial discretization, triangular elastoplastic shell elements were used with 11 integration points in thickness direction with an

Table 4
Parameters used for the pressure dependent part of the friction model given by Eq. (5). Since the dependence of the velocity was neglected, the corresponding parameters are not determined.

μ_0 [-]	p_0 [MPa]	ε [-]
0.46	1	0.36

element size of $1.25mm$. The mesh size was determined based on a convergence analysis with mesh sizes in the interval $[0.25mm, 5.0mm]$ in steps of $0.25mm$. The mesh size of $1.25mm$ was identified as the largest one with a relative difference $< 1\%$ w. r. t. the maximum occurring principal stress compared to the smallest mesh size. Furthermore, a relative difference of 0.3% (in absolute terms $< 0.1mm$) was observed w. r. t. the average draw-in in $0°$, $45°$ and $90°$ direction. A mesh size of $1.25mm$ was therefore found to be suitable for the simulation. Note that no mesh refinement was used, meaning that every node before forming can be assigned to a node at the end of the process. The movement of any arbitrary point throughout the process can therefore be determined by interpolating between the nodes, as will be shown later on. The interpolation based on barycentric coordinates used for this task is outlined in Section 3.2. The simulation includes a springback calculation at the end to simulate the elastic deformation after removal of the part.

3. Computational framework used in this work

3.1. Generation of synthetic data

The first objective of this work was to create a data set which allows for the identification of the most relevant areas in the part in terms of its material flow. Since sensitivity analysis and surrogate modelling require the evaluation of ≈ 100 experiments in this specific case, the data set for surrogate modelling was generated by a stochastic finite element

simulation. The number of required data points was based on 3 independent parameters of the stochastic FEM simulation, a factor of 2 since the inverse models use the radial and axial coordinates as independent model inputs, the usage of 6 folds during cross validation, test set size of 30% of the data points and a determination factor of 2, leading to an estimation of at least $n = 28 \cdot (\frac{6}{5}) \cdot (\frac{1}{0.7}) \cdot 2 = 96$ required data points. The cup-drawing process was parametrized with the same three independent parameters as the experiment shown in Fig. 6. These three parameters are summarised in Table 5 with their range used in the simulation. The DoE for the set of simulations was then determined using latin hypercube sampling as proposed by McKay et al. (1979) with $n = 100$ simulations, using equally spaced latin hypercubes, resulting in the sampled data points visualized in Fig. 8. A matrix P was built which contains each of the m input parameters for each of the n simulations, resulting in a dimension of $n \times m$.

After performing the simulations, two types of data were extracted. First, local thinning was used as quality criterion according to Eq. (6), where t_{init} and t_{end} represent the local material thickness before and after the drawing operation, respectively. This quality criterion was selected since it can be determined accurately in the simulation and in reality, and it provides an approximation of how far the cup is from failure. No wrinkling criterion was used, since the data-driven approach used in this work requires an exact quantitative evaluation in the simulation, which is not feasible for wrinkling, but is subject of ongoing work. Local thinning was evaluated at the top and in the sidewall of the cup in 90° intervals to rolling direction, resulting in 5 locations in total as can be seen in Fig. 9. Thinning was evaluated in the simulation in the green boxes visualized in Fig. 9 and averaged for each box to smooth local numerical errors. This data was then stored in a matrix Q of dimension $n \times t$ with n and t being the number of simulations and quality criteria, respectively.

$$thin = \frac{t_{end} - t_{init}}{t_{init}} \qquad (6)$$

Second, the position of the 21357 nodes in all three cartesian coordinates were extracted for each simulation for the initial sheet and the finally drawn cup, resulting in the matrices X_{init} and X_{final} of dimension $n \times 3s$ with n denoting the number of simulations and s the number of nodes. To interpolate between the nodes of the mesh, barycentric coordinates were used, which are briefly explained in the following section.

3.2. Interpolation between nodes using barycentric coordinates: Introducing the notion of SPM

To describe the deformation during forming, the notion of surface point markers (SPM) is introduced in the following. The authors refer to SPMs as points that do not move relative to the sheet during forming and whose displacement can be measured to obtain the material flow at any arbitrary location on the sheet. Fig. 10 visualizes schematically the concept of SPMs and their displacement $u = [u_r, u_z]$ from the beginning to the end of the drawing operation in 2D. The right side in Fig. 10 visualizes the displacements $u^{(1)}$ and $u^{(2)}$ for two different configurations (1) and (2), corresponding to two sets of input parameters $p^{(1)}$ and $p^{(2)}$ which differ by δp. Modelling the drawing process as a function G mapping from the input parameters p to the resulting displacements u, Fig. 10 visualizes that the change in the input parameters δp propagates

Table 5
Independent parameters and their range used for the stochastic finite element simulation.

Parameter	Min	Max
Blank holder force	$80kN$	$300kN$
Initial sheet position in X direction	$-4mm$	$4mm$
Initial sheet position in Y direction	$-4mm$	$4mm$
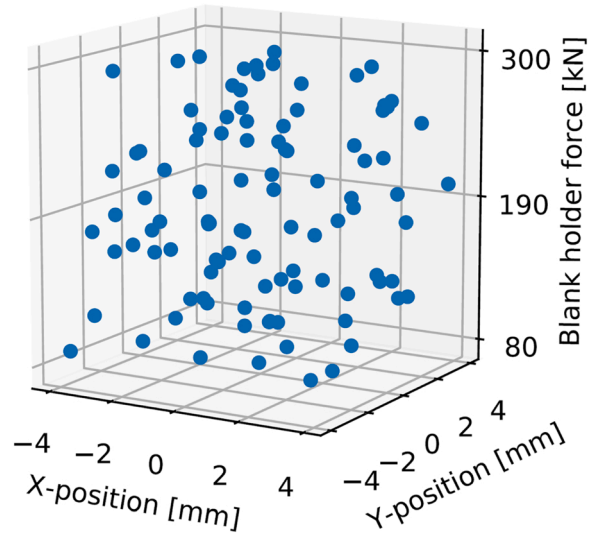
Fig. 8. Design of experiments based on latin hypercube sampling. Each data point corresponds to one simulation in the data set used for sensitivity analysis.

into a change of the displacements of each SPM given by δu and a change in sheet thickness at given locations δt. The general idea is to invert the mapping G, so that the displacement $u^{(i)}$ can be used to observe the process parameters $p^{(i)}$ in an inverse manner and then to observe quality criteria like the sheet thickness $t^{(i)}$ too.

Although the position of the SPMs does not change relative to the sheet during forming, their initial position can be defined in two different ways, which are in a frame of reference defined by the tools and one defined by the sheet. Differences between the two occur if the initial position of the sheet is alternated. The former one is more suitable for sensitivity analysis, since it eliminates the movement of SPMs simply caused by alternating the initial position of the sheet, whereas the latter one is actually present in the practical use-case if multiple sheets are marked with the exact same pattern. Accordingly, the former one was used during sensitivity analysis and the latter one afterwards for the model-based prediction of parameters and quality criteria in the experimental case.

In order to determine the material flow at any given location, SPMs were defined on the initial sheet as a function of the nodes in 3D space for each simulation using barycentric coordinates. For each SPM i, the barycentric coordinates correspond to the weights $m_{i,A}$, $m_{i,B}$ and $m_{i,C}$ such that the conditions given by Eqs. (7) and (8) are fulfilled. A_i, B_i and C_i correspond to the nodes of the triangular element in which the SPM i is located and $f_{init,i}$ describes the vector of the initial position of SPM i. One or multiple barycentric coordinates are negative if and only if the SPM lies outside of the triangle defined by the three nodes A_i, B_i and C_i. This property was used to identify the element of the mesh in which each SPM is located in the first place. Instead of using the node positions directly, the interpolation based on barycentric coordinates was used since it allows the determination of the material flow at any given location on the sheet, including between the nodes.

$$f_{init,i} = m_{i,A} \begin{bmatrix} A_{i,x} \\ A_{i,y} \\ A_{i,z} \end{bmatrix}^T + m_{i,B} \begin{bmatrix} B_{i,x} \\ B_{i,y} \\ B_{i,z} \end{bmatrix}^T + m_{i,C} \begin{bmatrix} C_{i,x} \\ C_{i,y} \\ C_{i,z} \end{bmatrix}^T \qquad (7)$$

$$m_{i,A} + m_{i,B} + m_{i,C} = 1 \qquad (8)$$

The barycentric coordinates $m_{i,A}$, $m_{i,B}$ and $m_{i,C}$ were determined on the initial sheet and then used by applying Eq. (7) for each SPM to interpolate its current position on the deformed part $f_{final,i}$. In a subsequent step, $f_{init,i}$ and $f_{final,i}$ for each SPM i and each simulation were then stored in the two matrices F_{init} and F_{final}, containing the position of each
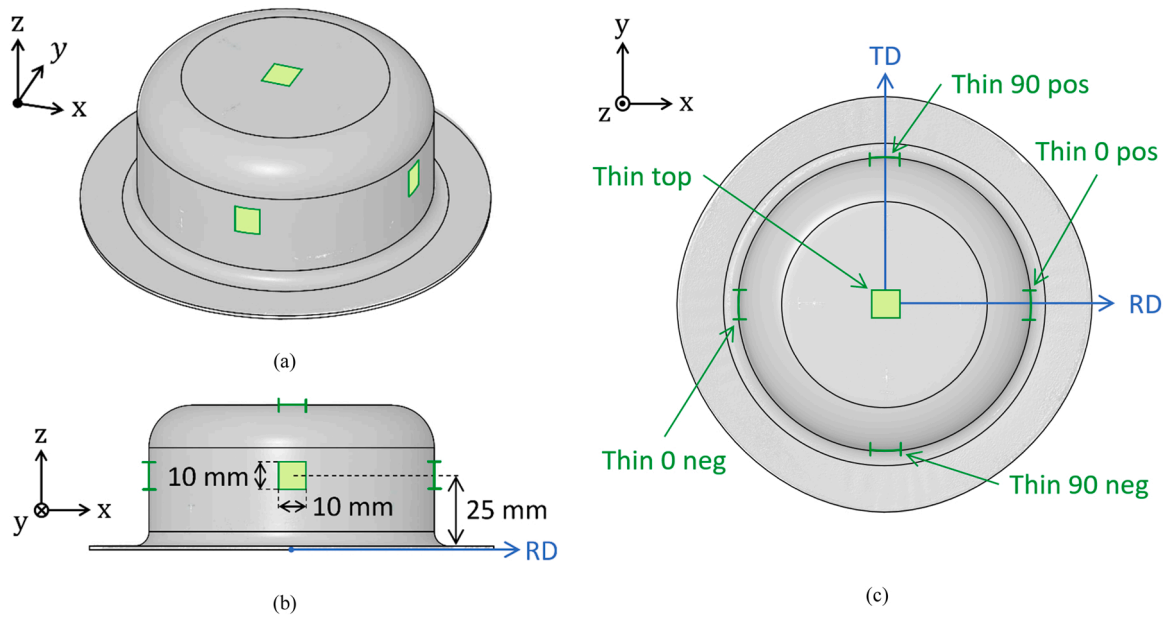
Fig. 9. Locations where wall thinning was evaluated (average in green area) in the simulation. In the experiment, the measurement is done in the middle of each square with the microscope. Thinning is evaluated in positive and negative direction to RD and TD, thus five times in total for each part. As illustration, the experimental result is used in the background, and contour lines as well as beginning and end of radii are marked with black lines.
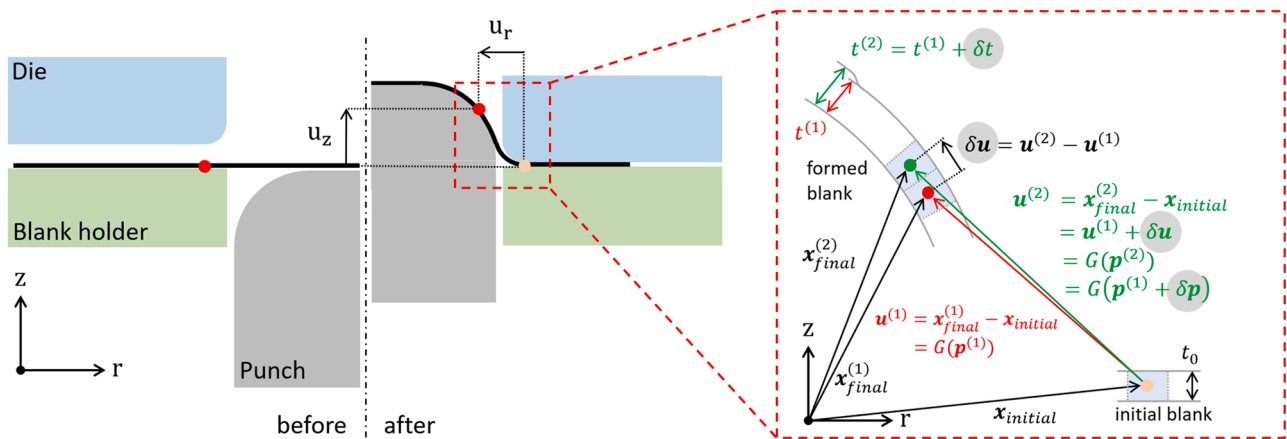
Fig. 10. 2D-visualization of the notion of surface point markers (SPMs). The red dot remains fixed relative to the sheet and its movement can be described by a vector by subtracting the initial positions from its final position, resulting in the components u_r and u_z. In contrast to the well-known draw-in measurement, the concept of SPMs allows the characterization of the material flow at every location on the sheet.
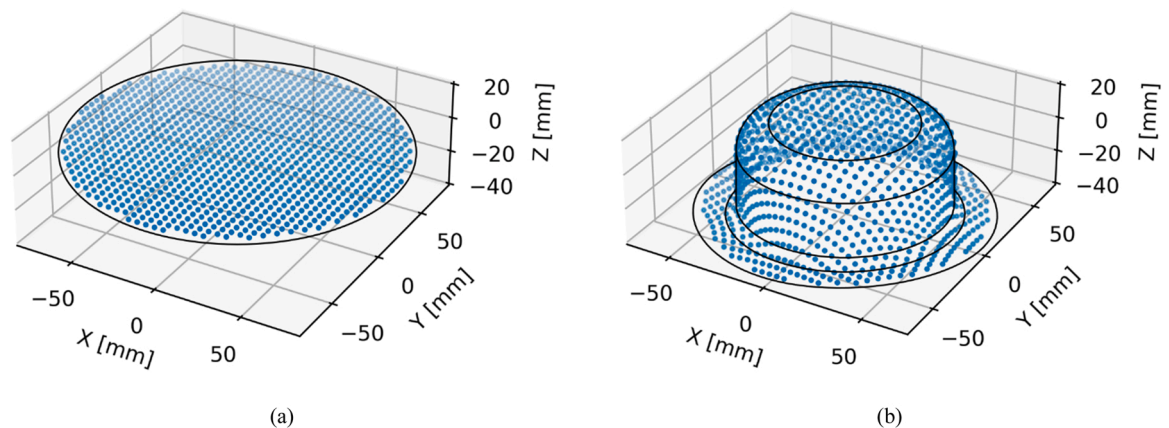
Fig. 11. Visualization of the 1041 SPMs used on the initial (a) and deep drawn part (b).

SPM in the initial and final configuration for each simulation. The displacement vectors for all SPMs and all simulations were then calculated by the spatial difference from before and after forming and stored in a matrix U of dimension $n \times (3e)$ with e and n being the number of SPMs and simulations, respectively. To ensure comparability of the simulations, the initial position of the SPM-grid was positioned identical relative to the tools for each simulation, meaning that their position relative to the sheet changes if the initial position of the sheet is alternated. This corresponds to the case in which the frame of reference is defined by the tools. The SPMs were defined in a mesh with an edge length of $5mm$ within a radius of $90mm$, resulting in 1041 points in total. It must be noted that since the SPMs are located within a radius of $90mm$ and the radius of the sheet is $95mm$, it is ensured that even if the initial position of the sheet is shifted by $4mm$, all SPMs always lie within the sheet. The location of the points is visualized in Fig. 11 on the left for the initial and on the right for the final configuration.

Since the cup-drawing is approximately a radially symmetrical process despite the effect of the material anisotropy and eccentric positioning of the blank, the coordinates of the SPMs were transformed into cylindrical coordinates. Fig. 12 shows the occurrence of the angular movement for all simulations and all SPMs in the data set. 95.0% of the SPMs in total contain an angular movement of $< 3°$, therefore the angular component of the node movement was neglected since it would not be in the measurable range in reality using the measurement methods used anyway.

3.3. Sensitivity analysis: Identification of optimal measurement positions of material flow

To identify suitable measurement locations of the material flow, sensitivity analysis was performed. In the general case, sensitivity analysis assesses how variations in the model output can be attributed to variations in the model input as outlined in more detail by Saltelli et al. (2008) (page 1). In this case, input and output correspond to the process parameters P and displacement vectors of the SPMs in U, respectively. Sensitivity analysis then enables to determine which proportion of the variation of the displacement vectors in U is caused by each of the process parameters in P. The goal is then to select at least one SPM containing maximum sensitivity towards each of the process
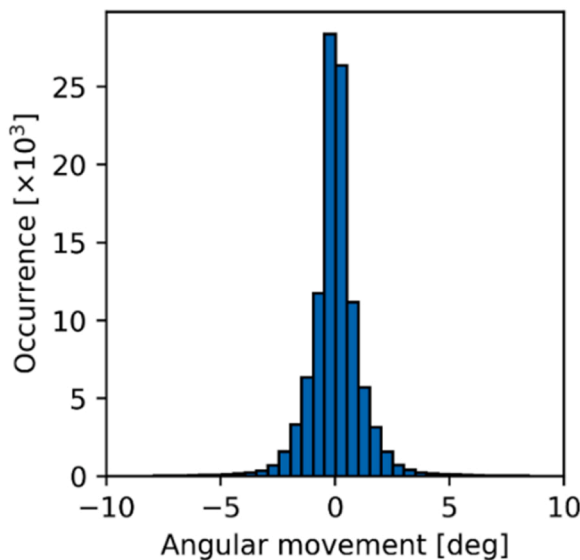
Fig. 12. Visualization of the angular variation of the displacement of each of the 1041 SPMs for each of the 100 simulations. Due to the radial symmetry of the part, 95% of the SPMs show an absolute angular displacement of $< 3°$. The angular component of the displacement was therefore neglected, since it would not lie in the measurable range anyway.

parameters. In the following paragraphs, the procedure used for the decomposition of the variance of the displacement of each SPM is explained, since the combination of these methods (i. e. Eq. (19)) have not been reported in the literature.

Consider again the cup-drawing process as a surrogate model of the form

$$\widehat{U} = G(P) = G(p_1, \ldots, p_m) \tag{9}$$

in which P describes the set of input parameters in normalized form and $\widehat{U}$ the modelled displacements of each SPM in 3D space. In our work, the python library Scikit-learn v0.21.1 provided by Pedregosa et al. (2011) was used for all surrogate modelling related tasks. If $G(P)$ is integrable over the whole parameter space $[0,1]^m$ and the parameters p_1, $\ldots, p_m$ are mutually orthogonal, then the variance of the displacement of each SPM j in $\widehat{U}$ (this is done for each direction separately) can be uniquely decomposed into its components according to

$$\mathrm{var}[\widehat{u}_j] = \sum_k \mathrm{var}_k + \sum_k \sum_{i>k} \mathrm{var}_{ki} + \ldots + var_{12\ldots m} \tag{10}$$

with

$$var_k = var_{p_k}[E_{p_{\sim k}}(\widehat{u}_j | p_k)] \tag{11}$$

and

$$var_{ki} = var_{p_{k,i}}\left[E_{p_{\sim ki}}(\widehat{u}_j | p_k, p_i)\right] - var_k - var_i \tag{12}$$

as proven by Sobol (1993). In Eq. (10), $\mathrm{var}[\widehat{u}_j]$ describes the total unconditional variance of the displacement of SPM j, var_k the variance contribution of p_k representing the variance of $\widehat{u}_j$ solely caused by p_k, var_{ki} the variance contribution solely caused by the interaction between p_k and p_i, and so on. Dividing Eq. (10) by the total variance $\mathrm{var}[\widehat{u}_j]$ for each SPM leads to

$$1 = \sum_i S_i^{(j)} + \sum_i \sum_{k>i} S_{ik}^{(j)} + \ldots + S_{12\ldots m}^{(j)} \tag{13}$$

where $S_i^{(j)}$, $S_{ik}^{(j)}$, ... represent the proportional contribution of each input p_i and each interaction term of the inputs on the total variance of the displacement of SPM j. The first order sensitivity indices $S_i^{(j)}$ describing the direct influence of each input on the displacement of SPM j are thus given by

$$S_i^{(j)} = \frac{var_i}{\mathrm{var}[\widehat{u}_j]} = \frac{var_{p_i}[E_{p_{\sim i}}(\widehat{u}_j | p_i)]}{\mathrm{var}[\widehat{u}_j]} \tag{14}$$

Note that the Sobol indices $S_i^{(j)}$ fulfil the conditions given by Eqs. (15) and (16) and that Eq. (16) is fulfilled with equality if and only if all interaction terms in Eq. (13) are equal to zero. In our work, the Python library SALib v1.4.5 provided by Herman and Usher (2017) was used to calculate the Sobol indices.

$$0 \leq S_i^{(j)} \leq 1 \tag{15}$$

$$\sum_{i=1}^m S_i^{(j)} \leq 1 \tag{16}$$

Eq. (14) shows that $S_i^{(j)}$ provides only a qualitative comparison of the contribution of each input p_i to the total variance $\mathrm{var}[\widehat{u}_j]$ due to the division by the numerator. To determine the quantitative influence of each input, the sensitivity indices given by Eq. (14) were scaled up by the total variance of the displacement of each SPM $var[u_j]$ in the data set given by Eq. (17).

$$var[u_j] = \frac{1}{n-1} \sum_{k=1}^n \left(u_j^{(k)} - \overline{u}_j\right)^2 \tag{17}$$

Since the sensitivity indices given by Eq. (14) are determined on a surrogate model which might be subject to errors, the accuracy of the

model has to be taken into account as well. Therefore, the coefficient of determination was used in its most general form given by

$$R^2 = 1 - \frac{\sum\limits_{k=1}^{n} \left(u_j^{(k)} - \widehat{u}_j^{(k)}\right)^2}{\sum\limits_{k=1}^{n} \left(u_j^{(k)} - \overline{u}_j\right)^2} \tag{18}$$

where $u_j^{(k)}$ represents the displacements in the data set, $\widehat{u}_j^{(k)}$ the predicted displacements and $\overline{u}_j$ the mean value of the displacements in the data set. Assuming that the variance in the data set is equal to the corresponding variance of the predictions and that the R^2 scores are sufficiently high such that they can be neglected due to the multiplication by 1 (only for illustration purpose here), Eqs. (14), (17) and (18) can be used to evaluate its product as

$$C_i^{(j)} = S_i^{(j)} \cdot \text{var}\left[u_j\right] \cdot R^2 = \frac{\text{var}_{p_i}\left[E_{p_{\sim i}}\left(\widehat{u}_j | p_i\right)\right]}{\text{var}\left[\widehat{u}_j\right]} \cdot \text{var}\left[u_j\right] \cdot R^2 \approx \text{var}_{p_i}\left[E_{p_{\sim i}}\left(\widehat{u}_j | p_i\right)\right] \tag{19}$$

which will be referred to as sensitivity product to estimate the variance caused by each process parameter i on the displacement of each SPM j for each direction independently. $C_i^{(j)}$ can intuitively be understood as a decomposition of the total variance of the displacements in U into the components caused by each of the independent input parameters. Note the qualitative behaviour of $C_i^{(j)}$ dependent on its components. All components of $C_i^{(j)}$ are for the general case positive and their product is zero if and only if one or multiple components are zero. $C_i^{(j)}$ decreases with decreasing $S_i^{(j)}$, decreasing modelling accuracy R^2 and decreasing variance of $\text{var}\left[u_j\right]$.

3.4. Algorithmic determination of measurement positions and fitting of inverse models

The sensitivities were evaluated for the radial and axial direction independently, since the position of each surface point marker is only measured before and after the drawing operation, meaning that the individual trajectory over time is unknown. The directional sensitivities were merged into one scalar by summing them up for each SPM. The finally obtained sensitivity product of each parameter i on the movement of each SPM j is therefore given by

$$C_{i,sum}^{(j)} = C_{i,r}^{(j)} + C_{i,z}^{(j)} \tag{20}$$

After merging the sensitivity products for each SPM with Eq. (20), a matrix C of dimension $m \times e$ was created which contains the values given by Eq. (20) for each parameter (rows) and each SPM (columns). The task of finding the most independent locations to measure the

material flow can then be translated into the mathematical problem of finding the h most linearly independent columns in C, where h represents the number of SPMs to be selected. Gu and Eisenstat (1996) (algorithm 4 on page 6) proposed a deterministic algorithm which is proven to find these h columns. This algorithm was therefore used in this work. The algorithm checks all combinations of the first h column vectors and every other column vector for an increase in the linear independence if one column is switched with the latter one. In the algorithm, linear independence of the selected column vectors is quantified by the size of the smallest singular value, with a larger smallest singular value being equivalent to more independent column vectors. The most linearly independent vectors are therefore sequentially moved to the left side of the matrix. Fig. 13 visualizes this principle for $h = 3$.

After the identification of the most sensitive SPMs, the movement of the determined points in r and z direction was used to fit models mapping to the parameters in P and quality criteria in Q. Since these models map from the original process output to its input and the quality criteria, they are also referred to as inverse predictive models. For all modelling-related tasks, elastic-net-regularization with 2nd order feature transformation of the input was used. All hyper parameters were identified by cross validation. The whole computational workflow including the data matrices mentioned is summarised in Fig. 14.

4. Results

4.1. Sensitivity analysis of surface point markers

In the first part of this section, the intermediate and final results of the variance decomposition described in Section 3.3 are presented. Fig. 15 (a) visualizes the modelling score based on Eq. (18) for each SPM. For Fig. 15 and all following figures containing a colour bar, the maximum value in the colour bar in green represents the maximum value present in the figure for better readability. The average R^2 score achieved is > 0.99 with a standard deviation of ≈ 0.004 and a minimum value of ≈ 0.91. Since the R^2 score for each point equals the average between the surrogate models for the r- and z-direction, this result implies almost perfect approximation of the displacement vectors in (r, z)-space for most of the SPMs by the surrogate model. Worth noting is the fact that the displacement vectors are accurately predicted even at the radii of the die as well as the punch, where the movement is strongly nonlinear due to the curved shape of the tool.

The variance of the r and z entries of the displacement vectors according to Eq. (17) is visualized in Fig. 15 (b) and (c). These values represent the mean squared deviation of the displacement from its mean value for each of the components in (r, z) and therefore visualizes which areas in the part react sensitively towards a change of the three input parameters *in total*. Important to observe is the fact that the maximum
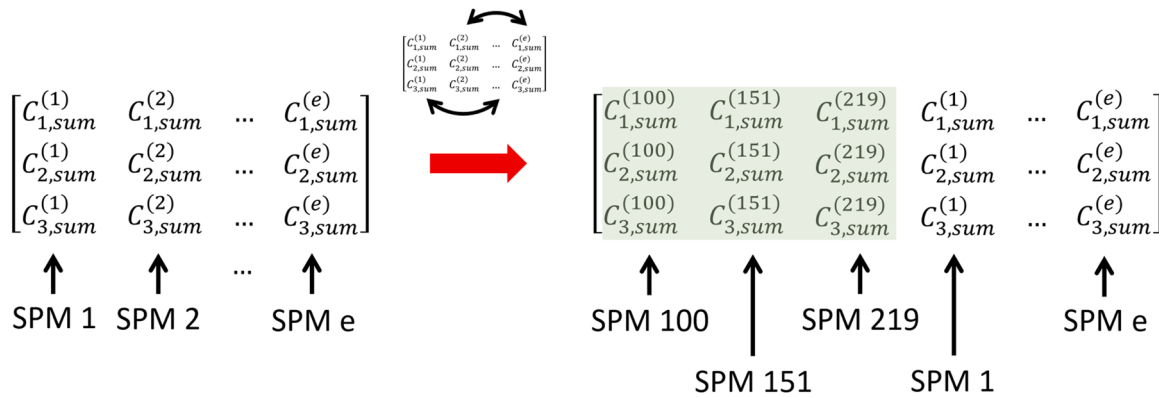

Fig. 13. Working principle of the subset selection algorithm to identify the most linearly independent column vectors. Each column contains the sensitivity products of all input parameters on the particular SPM. The task of finding the most independent SPMs then translates into the task of finding the most independent columns in the matrix highlighted in green on the right side.
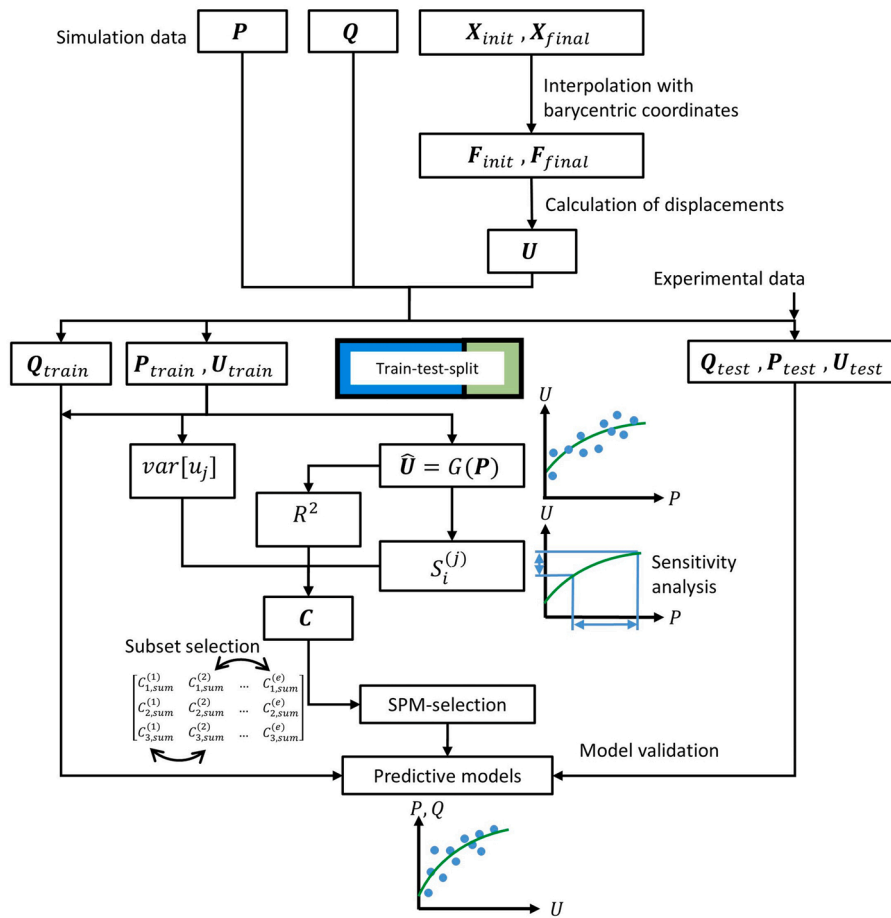
Fig. 14. Summary of the computational workflow used to first determine the most sensitive SPMs in the part and then train surrogate models to predict the input parameters and quality criteria as a function of the movement of the determined SPMs.
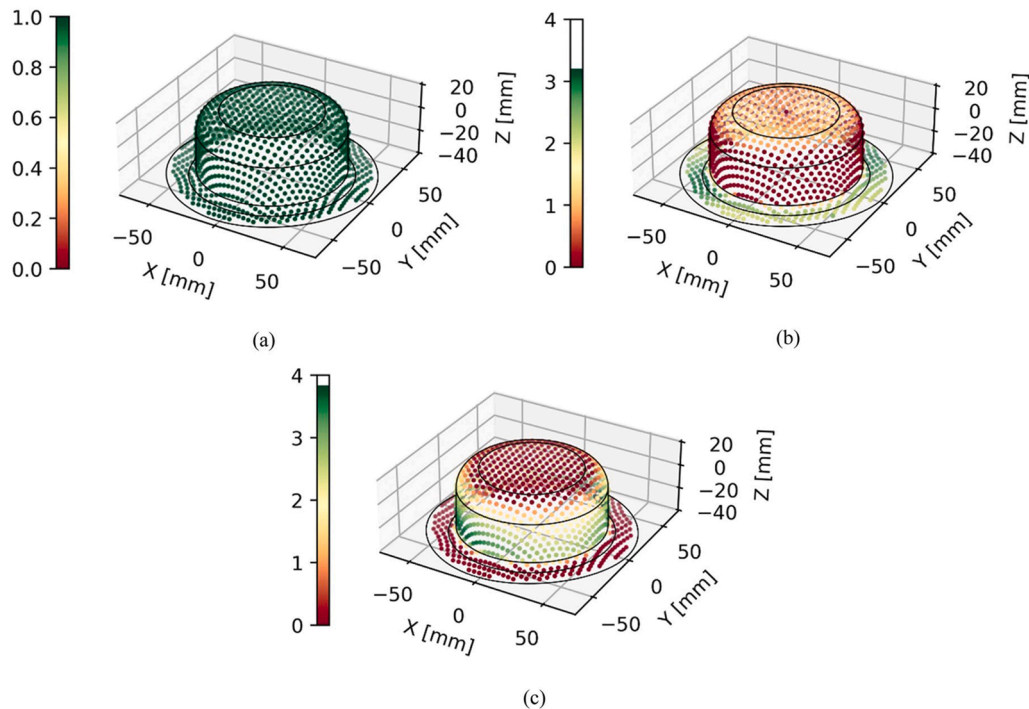

Fig. 15. Visualization of the R^2 score achieved during modelling (a), variance in radial (b) and axial (c) direction in $[mm^2]$ for each of the 1041 SPMs according to Eqs. (18) and (17), respectively.

occurring variance in the flange in radial direction is $\approx 3.21 mm^2$ whereas the corresponding value in the sidewall in z-direction is $\approx 3.84 mm^2$ and therefore $\approx 20\%$ larger. The maximum variance is obtained in the sidewall above the die radius (R5 in Fig. 4). Note that the changes in the initial position of the sheet do not directly influence the displacements of the SPMs since their initial position is defined in a coordinate system relative to the tools, meaning that their initial position is the same independent of the initial position of the sheet and the displacement vectors are affected by the deformation of the part only.

Fig. 16-Fig. 18 visualize the first order sensitivity indices $S_i^{(j)}$ according to Eq. (14) and the finally obtained sensitivity products $C_i^{(j)}$ according to Eq. (19) for each of the three input parameters. As can be seen in Fig. 16 (c) and (d) for the blank holder force, $C_i^{(j)}$ is largest in the die radius with a maximum of $\approx 0.27 mm^2$. The values decrease steadily towards the centre of the part as well as towards the sheet border. The distribution of $C_i^{(j)}$ over the part shows higher values for $C_i^{(j)}$ for the points on the Y axis despite the radial symmetry of the part. A reasonable explanation for this phenomenon lies in the material anisotropy. Since the points on the Y axis lie in transversal direction, the draw-in at this location and therefore the thickness is smallest in the flange. An increase of the blank holder force leads to the largest relative increase in this area. In fact, it can be observed in the simulation that the blank holder pressure increases in the middle of the flange in RD from $\approx 7 MPa$ to $\approx 30 MPa$, whereas it increases significantly more relatively speaking in TD from $\approx 2 MPa$ to $\approx 18 MPa$, hence the larger sensitivity. Overall, Fig. 16 (c) and (d) show that the decomposed contribution to the variance caused by a change of the blank holder force in the displacement vectors remains small with values below $0.3 mm^2$.

Fig. 17 visualizes the results of the sensitivity analysis for the initial position of the sheet in X direction. The sensitivity indices $S_i^{(j)}$ as well as the sensitivity products $C_i^{(j)}$ reach their maxima on the X axis and decrease monotonically during a rotation and reach their minima on the

Y axis, which results in the four quarter-like look if viewed from the top. Two important phenomena can be seen. First, the maximum value for $C_i^{(j)}$ of $\approx 2.96 mm^2$ is observed in the side wall right above the die radius, which is $\approx 29\%$ larger than the maximum value for $C_i^{(j)}$ obtained in the part flange. Second, although the SPMs located at the top of the cup on the X axis contain a sensitivity index of $S_i^{(j)} \approx 1$, the corresponding sensitivity product $C_i^{(j)}$ gets scaled down by the small values in radial direction as visualized in Fig. 15 (b) in that area.

Fig. 18 visualizes the results for the initial position in Y direction. The result is, as to be expected, qualitatively and quantitatively very similar to the results in Fig. 17 rotated by 90 degrees. The largest values for $C_i^{(j)}$ are again observed near the die radius, with decreasing magnitudes towards the centre of the part. The maximum value of $C_i^{(j)}$ is obtained on the Y axis in the lower part of the sidewall with $C_i^{(j)} \approx 3.04 mm^2$ which is $\approx 40\%$ larger than the largest value obtained in the part flange.

After merging the sensitivity products $C_i^{(j)}$ in Fig. 16-Fig. 18 (c) and (d) for both dimensions in the (r, z)-space with Eq. (20), the values for $C_{i,\text{sum}}^{(j)}$ for each parameter and SPM visualized in Fig. 19 are obtained. Additionally to the values on the final part geometry as previously, Fig. 19 contains the corresponding values visualized in the right column on the initial sheet. Two important results can be seen in Fig. 19. First, the maximum values of $C_{i,\text{sum}}^{(j)}$ are located either in, or directly above the die radius either at the X or Y axis for all three input parameters. $C_{i,\text{sum}}^{(j)}$ is decreasing towards the sheet border and towards the centre of the part. Second, the values for $C_{i,\text{sum}}^{(j)}$ obtained for the blank holder force are significantly smaller compared to the ones for the initial position in X and Y direction by a factor in the order of ≈ 10. As a side note, it can be seen in Fig. 19 that the movement of the SPM in the centre of the part contains no specific sensitivity to any of the parameters, which makes intuitively sense due to part symmetry.

Fig. 16. Visualization of $S_i^{(j)}$ [−] and $C_i^{(j)}$ [mm^2] according to Eqs. (14) and (19), respectively, for each of the 1041 SPMs resulting for the blank holder force. Left column corresponds to the component of the movement in radial and right column in axial direction.
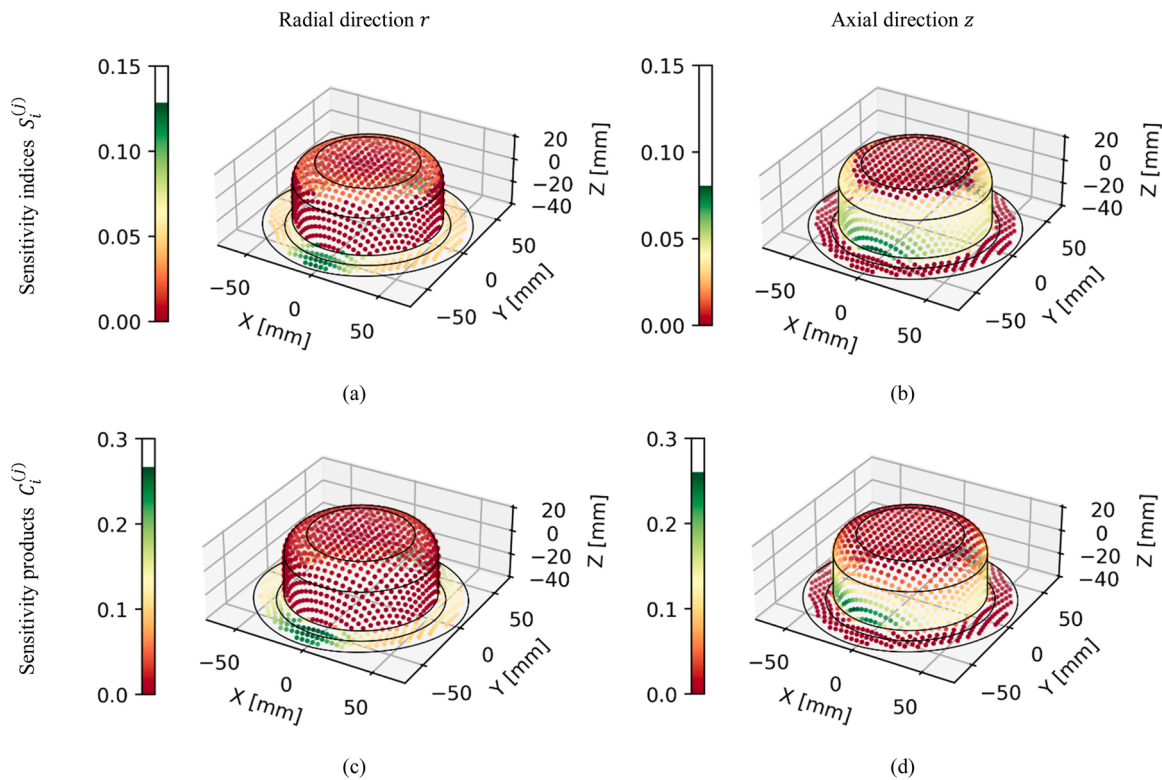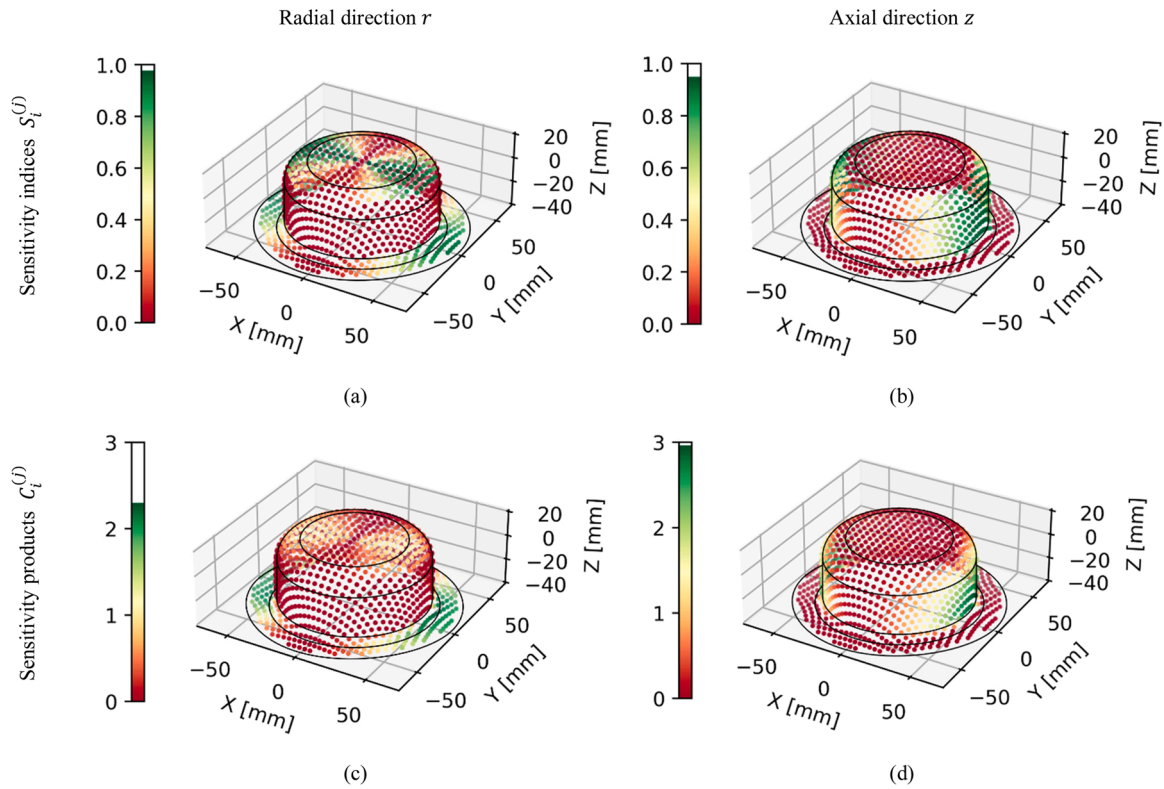
Fig. 17. Visualization of $S_i^{(j)}$ [−] and $C_i^{(j)}$ [mm^2] according to Eqs. (14) and (19), respectively, for each of the 1041 SPMs resulting for the initial position of the sheet in X direction. Left column corresponds to the component of the movement in radial and right column in axial direction.

Fig. 18. Visualization $S_i^{(j)}$ [−] and $C_i^{(j)}$ [mm^2] according to Eqs. (14) and (19), respectively, for each of the 1041 SPMs resulting for the initial position of the sheet in Y direction. Left column corresponds to the component of the movement in radial and right column in axial direction.
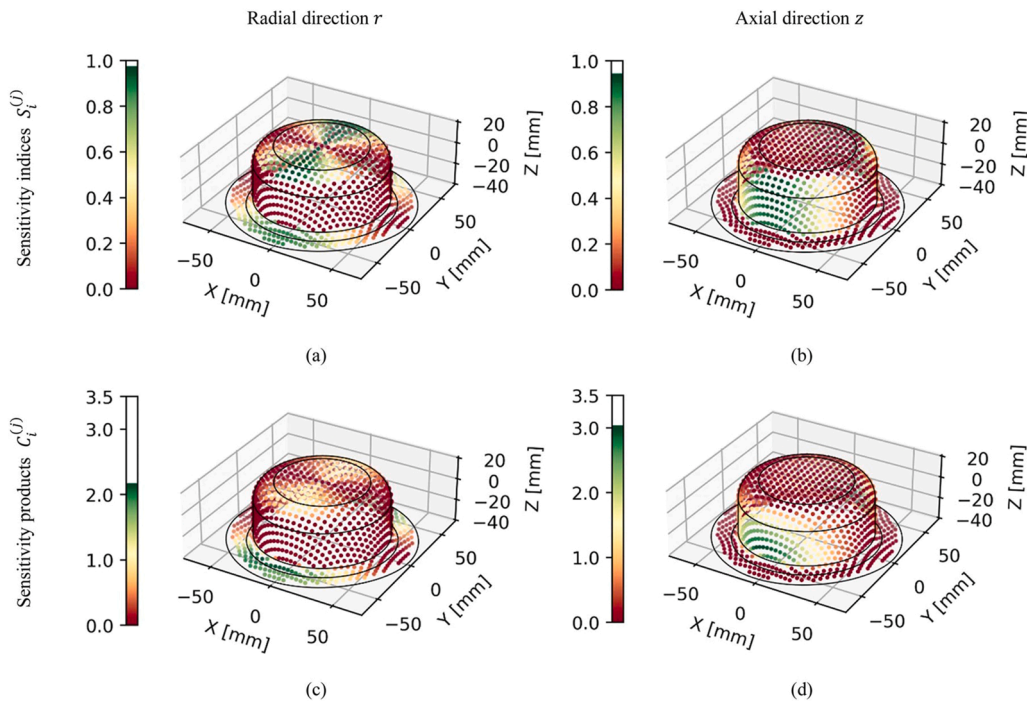
An overview over the maximum values for $C_{i,\text{sum}}^{(j)}$ obtained for each input parameter is given in Table 6. The data column on the left contains the maximum values as outlined above, which are all located in the lower part of the side wall. The subsequent two columns contain the maximum values considering the part flange and the sheet border only. The two columns on the right summarise the relative difference between the overall maximum value and the latter two. Table 6 shows that the
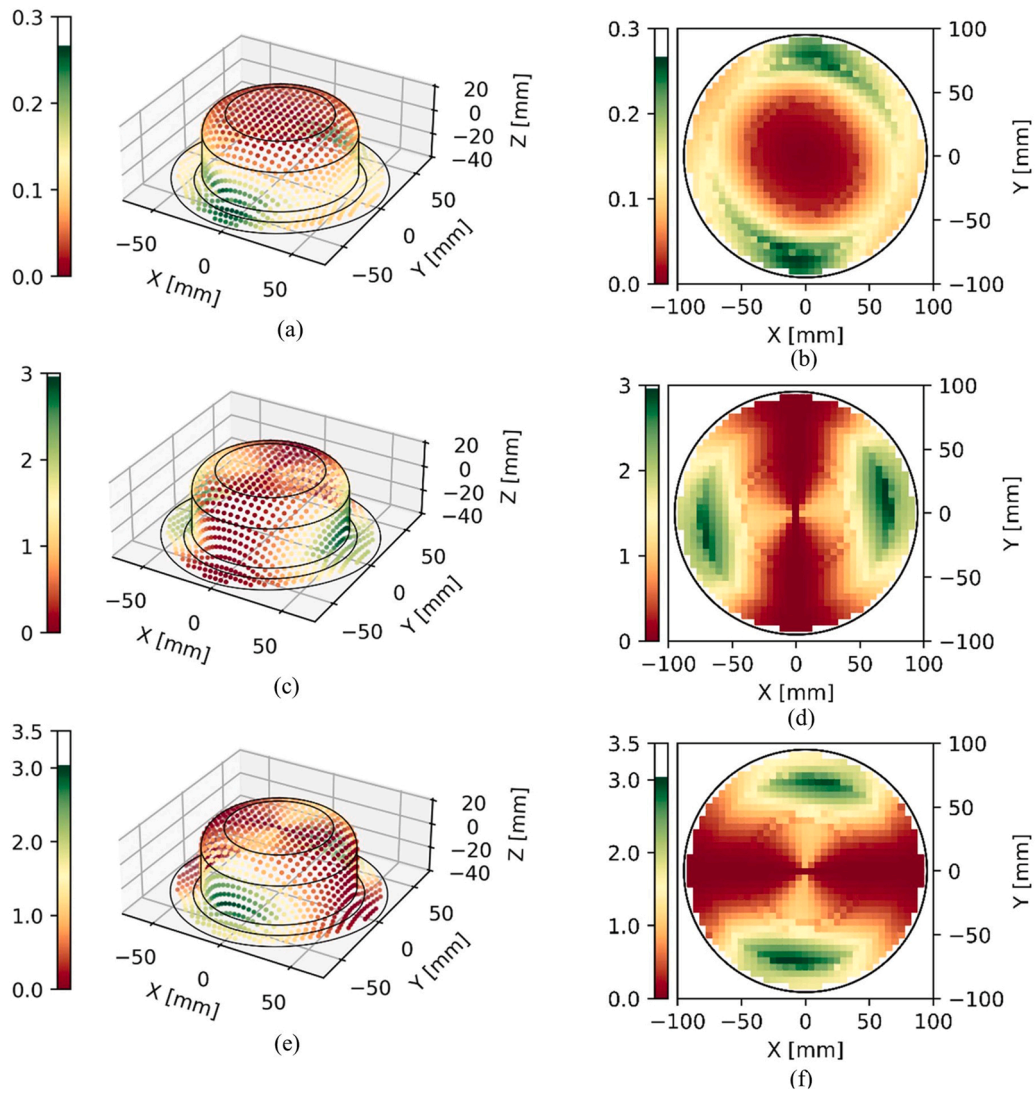
Fig. 19. Visualization of $C_{i,sum}^{(j)}$ [mm^2] with respect to blank holder force (a, b), initial position in X (c, d) and in Y (e, f) direction. In the right column, the corresponding values are visualized on the shape of the initial sheet. Values are calculated according to Eq. (20).

Table 6

Summary of the maximum values for $C_{i,sum}^{(j)}$ obtained according to Eq. (20) for different part regions.

Parameter	$Max(C_{i,sum}^{(j)})$ in the side wall [mm^2]	$Max(C_{i,sum}^{(j)})$ in the part flange [mm^2]	$Max(C_{i,sum}^{(j)})$ on sheet border[1] [mm^2]	Rel. diff. overall $max(C_{i,sum}^{(j)})$ to part flange [%]	Rel. diff. overall $max(C_{i,sum}^{(j)})$ to sheet border [%]
Blank holder force	0.27	0.27	0.23	+ 0.00	+ 16.0
X position	2.96	2.30	1.94	+ 28.7	+ 52.4
Y position	3.04	2.18	1.65	+ 40.0	+ 85.0

[1]Since the initial position of the sheet with radius of 95*mm* was alternated by $\pm 4mm$, SPMs on sheet radius lead to hanging (out of part geometry) nodes. Therefore, the SPMs representing the sheet border were evaluated at a radial position of 90*mm*, meaning that hanging nodes never occurred.

maximum sensitivity products obtained in the side wall are on average 23% and 51% larger compared to the maximum values in the part flange and on the sheet border, respectively.

4.2. Identification of independent measurement positions

After applying the subset selection algorithm on the matrix containing the merged sensitivity products $C_{i,sum}^{(j)}$ for each SPM as illustrated in Fig. 13, the most independent SPMs w. r. t. their $C_{i,sum}^{(j)}$ were determined. Since the number of points h to be selected by the algorithm is unknown at this stage, $h = 6$ was used as initial guess with 6 being equal to two times the dimension of the input space of the cup-drawing process in this case. The SPMs selected by the algorithm are visualized in Fig. 20 with the order denoted in red. Since the algorithm sorts the columns with decreasing linear independence, the order of the selected columns remains constant for different h, i. e. if the two cases $h_1 = 4$ and $h_2 = 5$ are considered, then the columns in the former case are identical and
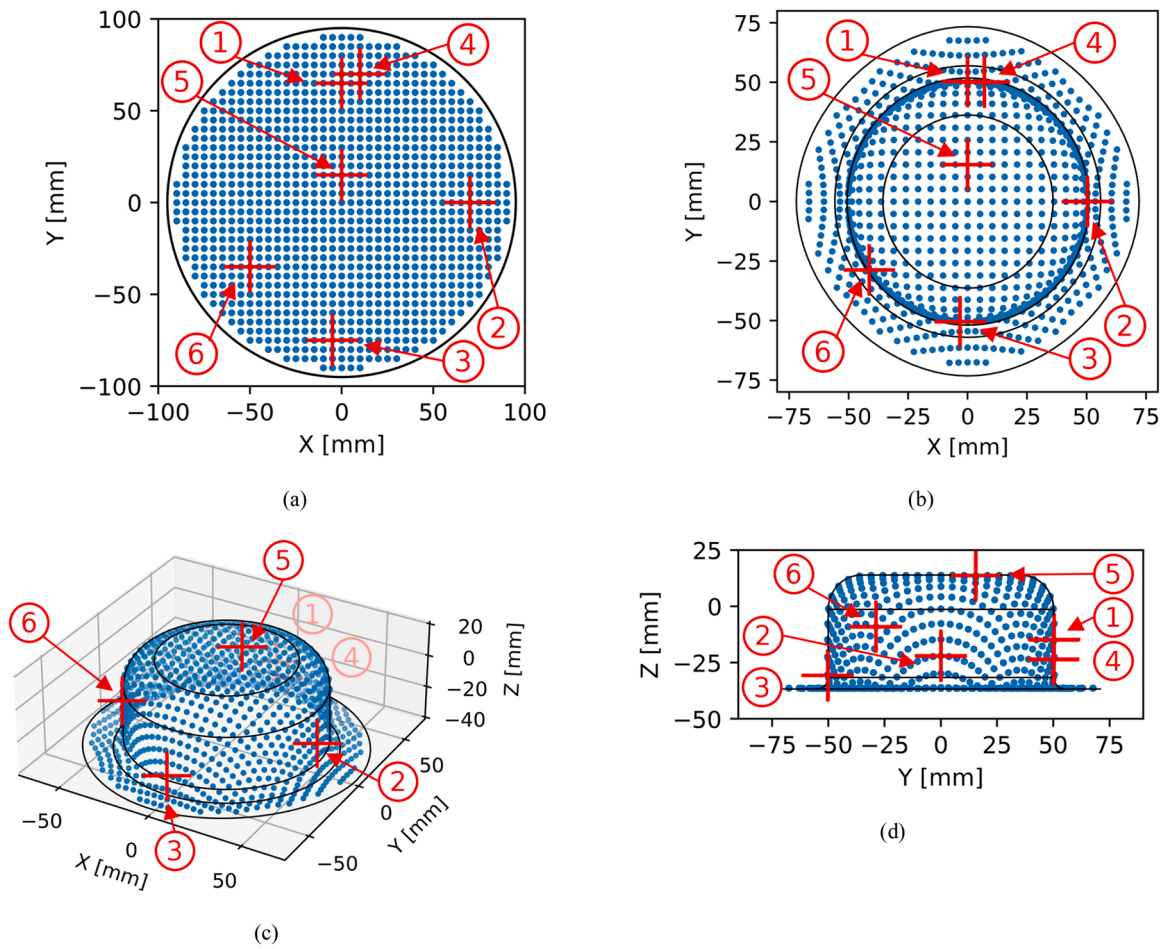
Fig. 20. Visualization of the six selected SPMs by the subset selection algorithm visualized in Fig. 13. Whereas (a) visualizes the positions on the initial sheet, (b)-(d) show the positions on the final cup. Numbers correspond to the order in which the SPMs are selected.

Fig. 21. Visualization of R^2 score achieved on the inverse surrogate model dependent on the number of SPMs for h = {1, 2, 3, 4, 5, 6} selected by the subset selection algorithm. (a) and (b) visualize mean, min and max scores achieved for the three input parameters and five quality criteria, respectively.

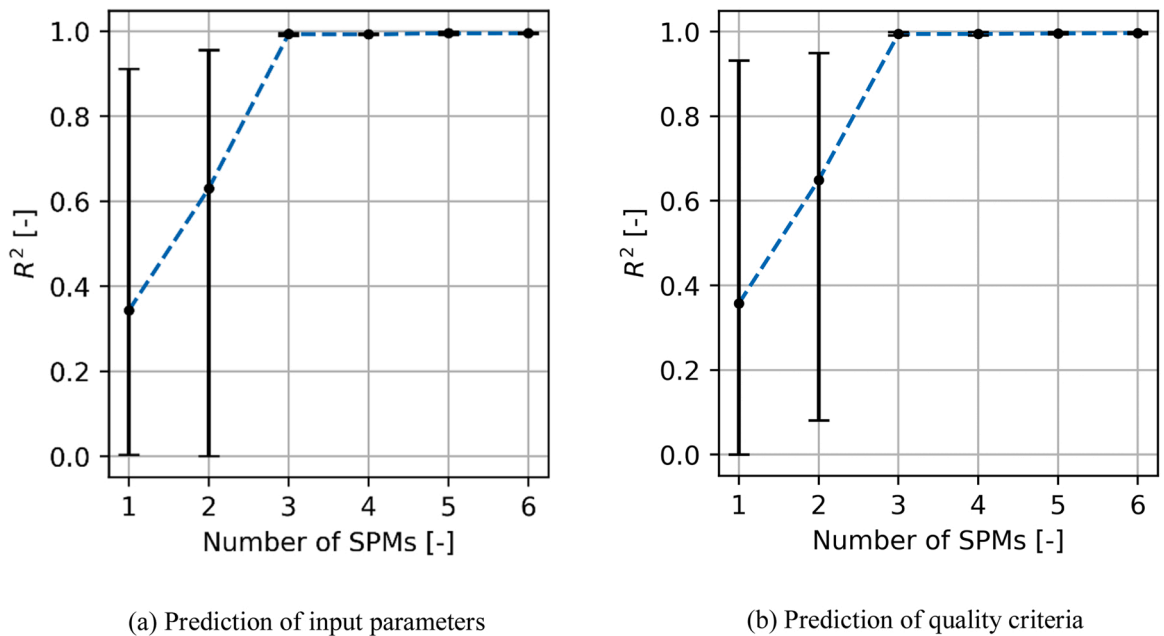selected in the same order as the first four columns in the latter case. Important to note is that due to stochasticity in the training set as well as numerical inaccuracies, the specific SPMs selected by the algorithm might alternate within the green areas visualized in the right column in Fig. 19. However, the characteristics of the points selected remain the same by being located in the green regions in Fig. 19.

4.3. Inverse modelling on the simulative data set

Using the displacement vectors of the determined SPMs in (r,z)-space as input, surrogate models were trained to predict the input parameters in an inverse manner and the thinning criteria shown in Fig. 9. The inverse models were then validated on the test set (30% of the simulations) as shown schematically in Fig. 14. The resulting minimum, mean and maximum values for each of the six cases of $h \in \{1, 2, 3, 4, 5, 6\}$ (i. e. $h = 2$ means using the first two SPMs visualized in Fig. 20) are summarized in Fig. 21. Fig. 21 shows that the result is very similar in both cases (a) and (b). The average R^2 score is 0.99 for $h = 3$, and only slightly increases to its maximum with $h = 4$ to almost $R^2 = 1.0$ and remains constant thereafter.

For the experimental study, the amount of SPMs was set to three ($h = 3$) based on Fig. 21. Since the precise location of the SPMs changes locally due to stochasticity and numerical inaccuracies, the SPMs were defined in the experiment on a radius of $R = 70mm$ on the initial sheet, which corresponds to the average of the radius of the three SPMs determined by the algorithm. The constant radius on the initial sheet will be used later on to compare the predictive accuracy with SPMs located at a different radius on the sheet. The location of the three SPMs determined by the algorithm as well as the three used for the modelling in the following are visualized in Fig. 22.

Using the three SPMs selected, Fig. 23 shows prediction and underlying truth for each data point in the simulative test set for all input parameters and thinning criteria. As expected based on Fig. 21 for $h = 3$, Fig. 23 shows an accurate prediction in all cases on the simulative test set.

4.4. Application of simulative models on the experimental data set

In a subsequent step, these models were applied on the experimental data set based on the DoE visualized in Fig. 6. The results are visualized in Fig. 24 analogously to Fig. 23. Note that due to the symmetry of the geometry, the initial positions were alternated only in positive direction to RD and TD in the experimentally obtained data set. Although a significant drop in the prediction accuracy was observed on the experimental data set, the model is still able to predict the overall tendency. On average, an R^2 score of 0.81 and 0.56 is achieved for the input parameters and quality criteria, respectively. Table 7 summarises the experimentally obtained results.

As can be seen in Fig. 24, most predictions are biased since the mean value of the predictions does not equal the mean value of the underlying truths. To further differentiate between systematic and non-systematic errors, the difference between the mean value of the underlying truths and the predictions was added to each predicted value in order to equalize the mean values of the two and the R^2 scores were calculated again. The third column in Table 7 contains the adjusted R^2 scores and the corresponding differences in the mean values are given in the fourth column. As can be seen, the average R^2 score improves to 0.86 and 0.73 for the parameters and the quality criteria, respectively, if adjusted for identical mean values. An additional error metric is provided in the subsequent column for the sake of comparability with literature and future work.

4.5. Comparison of different SPM positions

After determining the optimal locations for the SPMs, the predictive models were compared to the case if the position of the SPMs is alternated. For this, the displacement at additional locations was measured and the predictive accuracy of the inverse models compared. Fig. 25 visualizes the previously determined SPMs as black crosses in accordance to Fig. 22, and the additional locations as triangles on a radius of $R = 30mm$ and $R = 90mm$ on the initial sheet. Whereas the initial position $R = 30mm$ corresponds to the beginning of the punch radius at the top of the final cup, $R = 90mm$ corresponds to the most outer SPMs located near the sheet border, as can be seen in Fig. 25.

The predictive accuracy achieved on the simulative and experimental data set using the SPMs from Fig. 25 is visualized in Fig. 26. In the case of the simulative test set, almost perfect predictions are obtained using SPMs at the initial position of $R = 90mm$ and $R = 70mm$, with a small drop in the case of $R = 30mm$. On the experimental data set, a very low accuracy with an average R^2 score below 0.2 for the input parameters and sheet thinning is observed in the case of $R = 30mm$. The result obtained with the SPMs located at a radius of $R = 90mm$ lies in

(a)

(b)

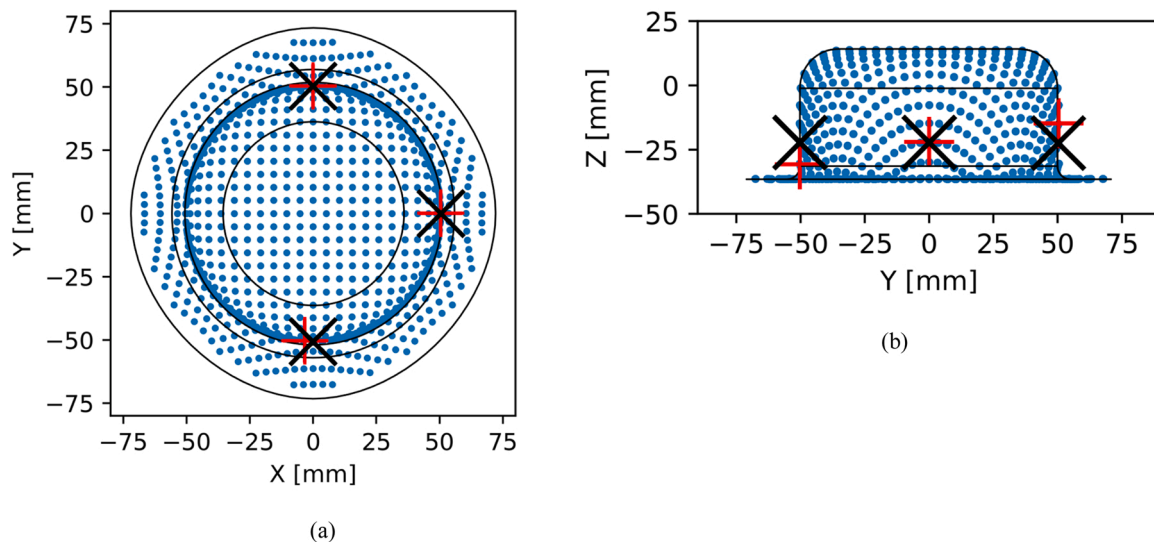**Fig. 22.** Visualization of the three SPMs determined by the algorithm (+) and the ones selected for the modelling (x) in the following. Due to stochasticity, the precise location of the SPMs determined by the algorithm varies. For the experiment, the points were determined on the X and Y axis on a radius of $70mm$ on the initial sheet, which is the average of the SPMs determined by the algorithm (see (b)).
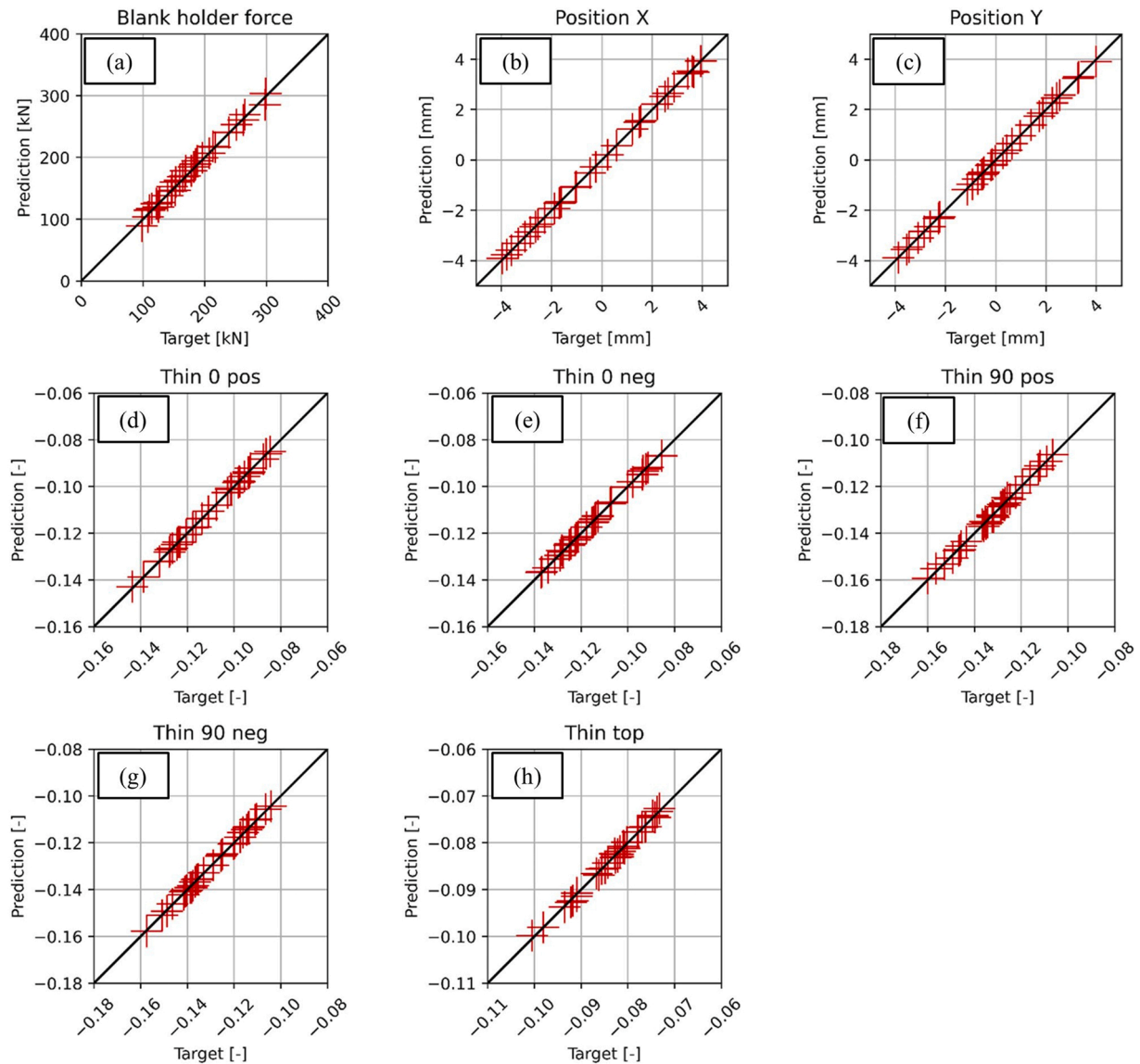
Fig. 23. Results of the inverse prediction for each of the input parameters and quality criteria using the three SPMs identified. The test set consists of 30 simulations not used during model training. All quantities are estimated with a R^2 score of 0.99 or higher. Location of sheet thinning in (d)-(h) see Fig. 9.

between the case of $R = 30mm$ and $R = 70mm$.

5. Discussion and interpretation of results

The results in Fig. 15 (a) show that the displacement vectors for all SPMs are modelled with a R^2 score close to 1. Its influence on the SPM selection given by Eq. (19) is therefore negligible due to its multiplication with the remaining expression. Nevertheless, the inclusion of the score is important for practical use, since it allows to punish surface point markers whose sensitivity analysis is based on a flawed surrogate model.

For the interpretation of Fig. 15 (b) and (c), the concept and interpretation of variance in this context has to be discussed first. The DoE given in Fig. 8 results in a change of the displacement vector u_j for each SPM j denoted by δu_j. The magnitude of u_j is not of importance per se, but the magnitude δu_j due to its sensitivity is, which is described here by the variance as metric. The variance can be interpreted by taking its square root which results in the standard deviation, having the same units as the underlying values, $[mm]$ in this case. Considering the SPM with the highest variance in Fig. 15 (c) and assuming a Gaussian distribution of the final position, the maximum standard deviation is $\approx$

$1.96mm$ directly above the die radius which results in $\approx 68\%$ data points being located within an interval of length $\approx 3.92mm$. This result gives an intuitive understanding about the total amount of variation that is present in the displacement vectors. The sensitivity product given by Eq. (19) can then be interpreted as a decomposition of the total variance into its parts caused by each of the three independent parameters.

As summarised in Table 6, the results show that for all three parameters, the SPMs with the highest sensitivity product $C_{i,\text{sum}}^{(j)}$ are located in the side wall, in or directly above the die radius. Furthermore, the distribution of $C_{i,\text{sum}}^{(j)}$ over the part in Fig. 19 (a) - (f) shows that $C_{i,\text{sum}}^{(j)}$ decreases monotonically with increasing and decreasing radial position. This result means that the material flow of surface point markers located in, or directly above the die radius reacts most sensitively to a change of the independent parameters. The result is partially consistent with the measurement locations for the material flow proposed by Griesbach (2000) (page 32 and 33). The author argues that since the main forming zones are given by first, the flange which consists almost exclusively of tension-compression stresses and second, the adjacent area around the die radius in which bending is superimposed with the tension-compression stresses, the most important measurement
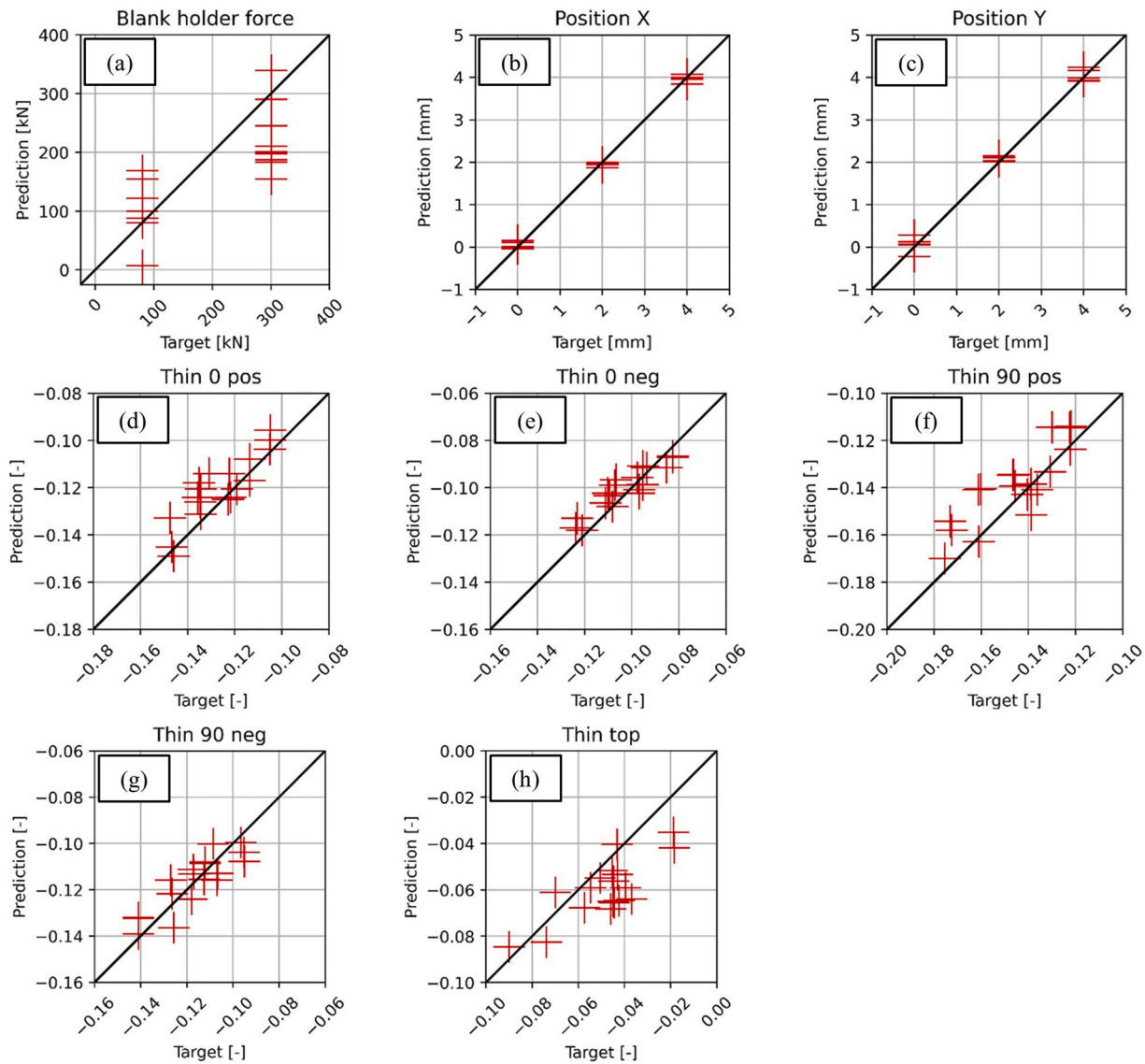
Fig. 24. Results of the inverse prediction for each of the input parameters and quality criteria using the three SPMs identified. The test set consists of the 18 experimentally created data points according to the DoE visualized in Fig. 6. During model training, the same simulative data set as in Fig. 23 was used. Results expressed in error metrics are provided in Table 7. Location of sheet thinning in (d)-(h) see Fig. 9.

Table 7

Prediction scores achieved on the experimental test set in Fig. 24 (MAE = mean absolute error, STD = standard deviation).

Predicted quantity	R^2 [−]	R^2 adj.[1] [−]	Offset adj.[1] [$kN/mm/-$]	MAE $\pm$ STD [$kN/mm/-$]
Blank holder force	0.45	0.58	− 39.92	70.28 ± 41.70
Position X	1.00	1.00	− 0.015	0.065 ± 0.054
Position Y	0.99	0.99	0.057	0.107 ± 0.076
Thinning 0° positive	0.57	0.75	0.006	0.007 ± 0.007
Thinning 0° negative	0.78	0.81	0.0022	0.005 ± 0.005
Thinning 90° positive	0.57	0.71	0.0065	0.009 ± 0.009
Thinning 90° negative	0.74	0.74	0.000	0.007 ± 0.007
Thinning top	0.14	0.62	− 0.012	0.014 ± 0.008

[1]The term adjusted refers to the R^2 score where the mean of the predictions is corrected by the difference to the mean of the targets.

locations to characterize the material flow are the ones with the most different stress states and therefore given by three locations: The material flow at the sheet border, at the beginning of the die radius with overlapping compressive stresses at the upper side of the sheet due to bending, and at the end of the die radius with overlapping tensile stresses. Note that the latter one corresponds to the area identified as previously mentioned. However, since the material flow at these three locations is almost fully correlated assuming constant azimuthal coordinate, the measurement at one radial position is sufficient as observable.

The second reference which provides a specific proposal for the measurement of the material flow is provided by Maier et al. (2017). The measurement of the skid-lines proposed by the authors, as described in Section 1 paragraph six, corresponds to the SPMs located at a height of $35 - 40mm$ due to the die radius of $15mm$. As can be seen in Fig. 19, these points contain a similar sensitivity product $C_{i,\text{sum}}^{(j)}$ as the ones on the sheet border, with the exception to the ones corresponding to the blank holder force visualized in Fig. 19 (a) where the values for $C_{i,\text{sum}}^{(j)}$ are approximately twice as large on the sheet border. The corresponding values for $C_{i,\text{sum}}^{(j)}$ are therefore significantly smaller than the maximum values in the side wall as can be seen in Table 6. Maier et al. (2017) argue in the introduction in a qualitative way, similar to Griesbach (2000), that the
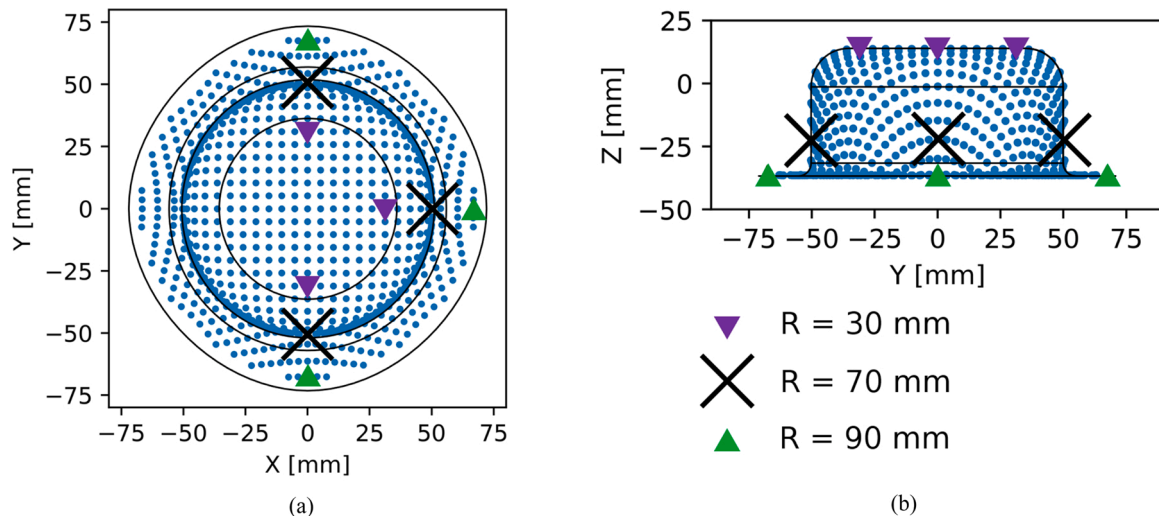
Fig. 25. Visualization of the three SPMs used in the experimental study as optimal values ($R = 70mm$), and the ones used for comparison ($R = 30mm$ and $R = 90mm$). The radius corresponds to the position on the initial sheet.
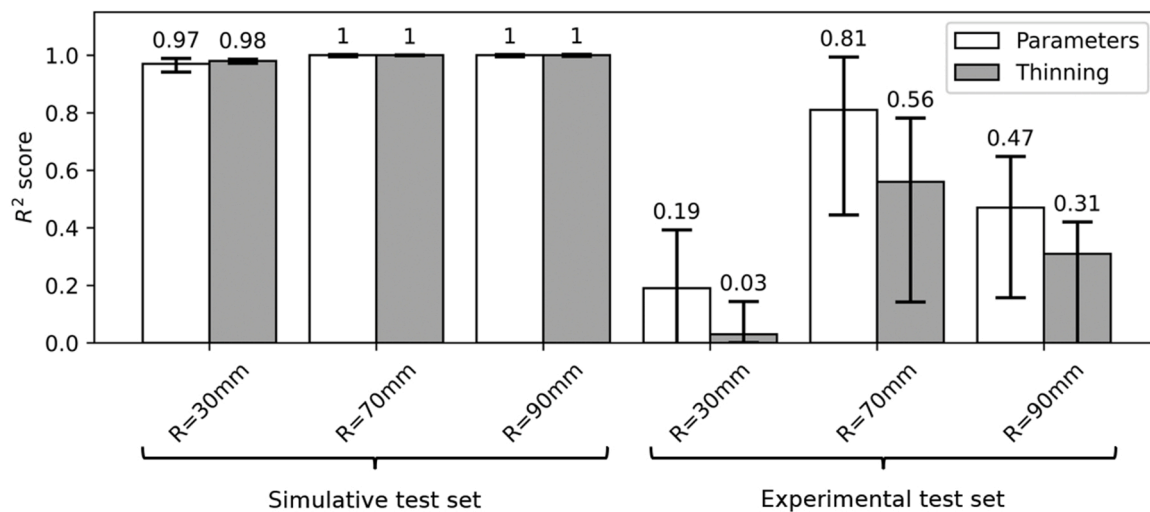

Fig. 26. R^2 scores achieved using the SPMs visualized in Fig. 25 on the simulative and experimental data set. Error bars visualize the range of the individual parameters and thinning criteria obtained. Numerical values on top represent the mean values visualized by the bars. Note that the results for $R = 70mm$ correspond to the results visualized in Fig. 23 and Fig. 24.

material flow should be measured in the main forming zones. Although our previously mentioned result is consistent with this claim, the proposed measurement locations given by the location of the skid-lines do not seem to be beneficial compared to the draw-in. However, since the location of the skid-line is dependent on the tool geometry, its location might be closer to the areas of highest variation in the material flow for different part geometries than the one used for the investigation here. Maier et al. (2017) also argue that whereas the draw-in is not measurable at the end of the press line since the sheet border gets usually cut shortly after drawing in a subsequent operation, the skid-line remains usually in the part throughout the whole process chain and thus the measurement can also take place at a later stage, which has definitely to be classified as an advantage of the skid-line measurement. Interestingly, since the surface point markers in our case lie in the actual part too, this advantage over the draw-in is valid for the concept of SPMs proposed in this work too. It must also be noted that our investigation was carried out on a simple cup geometry, while Maier et al. (2017) used for their investigations a side panel frame and an inner door panel. However, since the stress states in complex formed parts remain qualitatively similar to the simple cup drawing process, a loss of generality of

the results presented is not expected. This reasoning is confirmed by Griesbach (2000) on page 33.

Since the initial position in *X*- and *Y*-direction are the dominant influence factors as can be seen based on the large sensitivity indices in Fig. 16 - Fig. 18 (a) and (b), the first two SPMs selected by the algorithm in Fig. 20 correspond to the areas with highest sensitivity products towards these input parameters (point 1 and 2 in Fig. 20). The third SPM is selected such that it reacts sensitively towards the blank holder force, as can be verified by considering Fig. 19 (a) and (b) and Fig. 20 (b). However, the reason for the following three SPMs selected is not intuitively apparent, considering the fact that the fourth SPM lies in the immediate vicinity of the first one as can be seen in Fig. 20 (a) and the fifth is selected around the central axis of the cup where the sensitivity product $C_{i,\text{sum}}^{(j)}$ is almost zero w. r. t. all parameters. This observation is explained by the working principle of the algorithm which is visualized in Fig. 27. Fig. 27 illustrates the sensitivity products in the input parameter space for the first three SPMs selected by the algorithm. The objective of the deterministic subset selection algorithm by Gu and Eisenstat (1996) is to find the *h* linearly most independent column
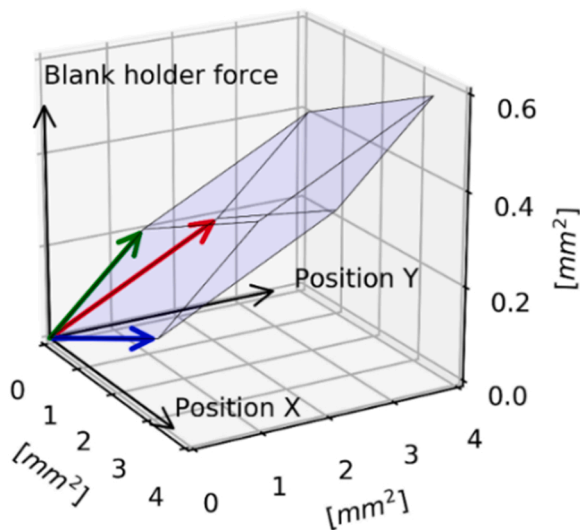
Fig. 27. Visualization of the sensitivity product vectors corresponding to the first (red), second (blue) and third (green) SPM in Fig. 20. The absolute value of the determinant which is maximized by the subset selection algorithm of the three vectors corresponds to the spanned volume of the parallelepiped.

vectors of the sensitivity matrix as shown in Fig. 13, which can be translated into maximizing the smallest singular value of the independent columns on the left side while minimizing the largest singular value of the dependent columns on the right side as outlined by Gu and Eisenstat (1996) on page 5. Since the determinant of the matrix containing the independent column vectors is calculated by the product of its singular values, what the algorithm is effectively doing is maximizing the determinant of the linearly independent column vectors, which can also be understood as maximizing the volume of the parallelepiped spanned as visualized in Fig. 27. Since the selected column vectors are per definition the most linearly independent ones and since the 3D space is spanned given three linearly independent column vectors, every column vector and therefore every SPM selected after the third one does not and cannot increase the determinant of the matrix containing the independent column vectors. Referring to Fig. 27, this implies that every subsequently selected column vector lies inside the volume of the parallelepiped. Since the determinant remains constant independent of which column vector is additionally selected, every SPM selected after the mth one with m being the dimension of the input space (three in this case) is arbitrary.

A comparison of the result on the simulative test set in Fig. 23 with the experimental one in Fig. 24 shows a clear drop in the accuracy of the model predictions from 1 to 0.81 and 1 to 0.56 (0.67 without the outlier given by thinning at the top of the cup) for the input parameters and thinning criteria, respectively. This decrease in accuracy can on the one hand be attributed to a systematic error between the simulation used for modelling and the experimentally obtained test set, which is confirmed by a comparison of the R^2 scores in Table 7 with the adjusted ones in the third column. On the other hand, measurement noise and inaccuracies in the experimental setup contribute to the decrease in prediction accuracy too.

Bringing the above mentioned points together, more insight into the relationship of the sensitivity of the movement of the SPMs used and the predictive accuracy of the models is revealed by Fig. 26 by comparing the modelling results for the SPMs with a radius of $30mm$, $70mm$, and $90mm$ on the initial sheet. As observed in Fig. 19, in combination with Fig. 26, it gets clear that the increase in the overall sensitivity of the SPM movement only barely translates into an increase of predictive performance in the case of the simulative test set. At the same time, the corresponding results obtained with the experimental test set profit significantly from the optimized positioning of the SPMs given by a

radius of $70mm$ in this work. Therefore, a clear positive correlation between the sensitivity metric given by Eq. (20) and the predictive performance of the inverse models is identified on the experimental test set. The reason for this result is that the larger sensitivity of the observable directly translates into a larger signal to noise ratio, assuming a constant measurement noise, which is less for the simulative test set where the amount of noise in the measurement signal is almost negligible. This result illustrates the importance of sensor selection in general, and why it is important to optimize for maximum sensitivity in the observable. Furthermore, it also highlights the importance of an experimental validation of the models since the representative power of the observables is usually not assessed by considering simulative data due to the lack of noise.

Finally, the results illustrated in Fig. 23 and Fig. 24 and in Table 7 must be put into context with literature. Literature provides, to the best knowledge of the authors, four references with comparable results. These are summarised in Table 8, including the new results from this study in the last two rows. Note that no reference was found containing quantitative predictions based on experimental data. Similar to the results Huang et al. (2016) obtained in their work with a cup geometry as used in this study, almost perfect accuracy is achieved on the simulation-based test set as a comparison with Fig. 23 shows.

The prediction results provided by Huang et al. (2016) are not based on classical observables like draw-ins, but rather on hardening curve parameters and the coefficient of friction. However, they are mentioned here since the hardening curve parameters can be determined for example by the eddy current principle as proposed by Heingärtner (2012) for exactly that use case, and the part geometry used is very similar to the one used in this work. The following three references listed in Table 8 use geometrically more sophisticated parts. Neuhauser et al. (2019) performed their investigation on a tailgate and achieved a prediction accuracy of 0.78 on average on a simulative test set. This R^2 is significantly lower compared to the one achieved in this work, as a comparison with the simulative test results shows. The reason for this result lies most probably in the geometrical properties of the part itself, since the flat shape of the tailgate leads to a large distance between the sheet border where the draw-in is measured, and the areas in the centre of the part where the quality criteria are determined. The authors hypothesize that specifically in that case, the material flow measurement in the main forming area might be highly beneficial, since the measurement of the material flow can be shifted much closer to the areas of the highest plastic deformation. This hypothesis has to be validated by applying the methodology on a more complex deep drawn part in future work.

Kott et al. (2021) provide the prediction accuracies for five different parts using different types of input variables. To compare them with our results in Table 8, the data provided by Kott et al. (2021) (in Table 6 in the reference) row ANN1 is used, since the sole use of the draw-in as observable is most comparable to our work. The average R^2 score achieved by the authors for all five parts is 0.90, using a simulative data set only. The result is most probably lower compared to our case (compared to the simulative results too) for the same reason as the results provided by Neuhauser et al. (2019). The higher R^2 score compared to the latter reference might be caused by the fact that the predicted output of the model is given by only one variable which is the maximum occurring max. failure value, as opposed to 22 different quality criteria used by Neuhauser et al. (2019).

Finally, Ryser et al. (2021) provide modelling results based on a side panel frame and thus the most complex part found in the literature. In this reference, the target variables are not quality criteria, but the input parameters of the process and are thus comparable to Fig. 23 and Fig. 24 (a) – (c). The average R^2 score for 21 input parameters is 0.93 with one outlier (≈ 0.98 without outlier). Neglecting the outlier, the result lies therefore in a similar range compared to the simulation results provided in Fig. 23.

Table 8

Overview over comparable results found in the literature.

Reference	Parts used	Predictor variables	Target variables	Type of test set	Average R^2 on test set
(Huang et al., 2016)	Cup	Flow curve parameters, friction coefficient	Max. punch force, min. sheet thickness	Simulation	1.00 / 0.98[1]
(Neuhauser et al., 2019)	Car tailgate	Draw-in	22 different quality criteria	Simulation	0.78
(Kott et al., 2021)	Five different car body parts	Draw-in[2]	Global max. failure[3]	Simulation	0.90[4]
(Ryser et al., 2021)	Car side panel frame	Draw-in, local blank holder force	21 Process and material parameters	Simulation	0.93
Presented work here	Cup	Displacement of selected surface point markers	3 input parameters and 5 quality criteria	Simulation	1.00 / 1.00[5]
Presented work here	Cup	Displacement of selected surface point markers	3 input parameters and 5 quality criteria	Experimental (Models trained by simulation)	0.81 / 0.56[5]

[1]Maximum punch force / minimum sheet thickness

[2]Reference also makes use of other predictor variables. Result with draw-ins is chosen since for the sake of comparability.

[3]Denotes the max. occurring ratio between maximum major strain and the major strain of the strain based FLC for the same minor strain among all elements.

[4]Average is chosen over all five parts for the best performing model type.

[5]Average of three parameters / average of five quality criteria

As summarised in Table 8 and elaborated more in the paragraphs above, a direct comparison of our experimental results with literature is not possible, as no directly comparable ones were found. The results here provide a first benchmark for future research papers. Furthermore, whether the prediction accuracy achieved in this work is sufficient for practical usage depends on the intended use case. As can be seen by a comparison of the R^2 scores with the adjusted ones in Table 8, potential can be identified in increasing the accuracy of the simulation, which will be of high relevance for the future and has recently been addressed for example by Chen et al. (2022).

6. Conclusion

In this work, the notion of surface point markers (SPMs) was introduced, which represents points fixed relative to the sheet whose displacement from the initial to the final configuration is measured. A novel algorithmic method is then presented to identify the most sensitive measurement locations for these points on a deep drawn part and applied on a cup drawing process. The method is validated based on a simulative and experimental data set, comparing differently positioned surface point marker locations.

The conclusions are summarised as follows:

1. Literature provides indications that the material flow in deep drawing should be characterized in the areas of the highest plastic deformation, as opposed to the sheet border given by the draw-in. This statement was investigated here for the first time in a quantitative way. In this study, an increase in the variance of the movement of material points in the areas of the highest plastic deformation of on average 51% was observed, compared to the draw-in at the sheet border. This result is in accordance with the indications in the literature mentioned previously.

2. The increase in sensitivity of the displacement of material points results directly in an increase of the modelling accuracy if quality criteria like local sheet thickness or the input parameters are modelled. More specifically, for material points located at three different radii 30*mm* / 70*mm* / 90*mm* on the sheet, the variance of 1.1*mm*^{2} / 3.0*mm*^{2} / 2.0*mm*^{2} caused by the change of the input parameters results in an average R^2 score of 0.03 / 0.56 / 0.31 for local sheet thinning and 0.19 / 0.81 / 0.47 for the inverse prediction of the input parameters, evaluated on the experimental data set. Therefore, a clear correlation between the sensitivity of the displacement of the SPMs and the predictive accuracy of the models is identified.

3. The areas of the largest sensitivity were identified in, or directly above the die radius, in the lower part of the side wall of the cup. As

pointed out in the literature by Griesbach (2000), this result can be generalized for complex shaped parts due to the qualitatively similar stress states during forming.

4. Application of a column subset selection algorithm allows the systematic determination of independent sensor positions. The method is computationally expensive due to the large set of FEM simulations required (100 in this case). However, the mathematical methods thereafter are currently not critical in terms of computational cost, which might make the method feasible for industrial use if the simulation time can be reduced.

The measurement of the material flow based on markings on the sheet is a promising approach to observe and control deep drawing processes, since their measurement requires no tool specific sensors, like laser sensors for draw-in measurements, or similar. Another advantage is the fact that this measurement method provides maximum flexibility due to its independence of the part geometry. This approach unfolds its full potential if it is coupled with simulation-based models as proposed here and enables the quantitative estimation of quality criteria. The results presented in this paper provide a feasibility study of the mathematical, simulative, and experimental methods applied on a simple deep drawn part. Application on a more complex part is required to prove or disprove the superiority of the method proposed for real applications and will be part of a future project and paper.

This paper shall be concluded with a brief discussion about the practical implementation. To this date, there is no specific measurement system or use case known, on an industrial level, in which the global material flow of sheet metal parts is measured inline. The first reference indicating industrial interest in this field was found in a news article by Markus Strehlitz (2015). The author describes the introduction of an inline quality control system in the press shop of a large automotive manufacturer. It consists of stripe projection scanners, which follow the same optical measurement principle as the scanner used in this work, mounted on robot arms. This setup allows the full digitization of stamped parts and evaluation of the surface topology directly in the production line to control quality. Equipping the measurement setup with a pattern recognition system would allow the localization of predefined patterns on the surface of the part. The authors expect future developments in this field.

CRediT authorship contribution statement

Matthias Ryser: Conceptualization, Data curation, Formal analysis, Investigation, Methodology, Software, Validation, Writing – original draft, writing – review & editing. **Pavel Hora:** Methodology,

Supervision, writing – review & editing. **Markus Bambach:** Supervision, writing – review & editing.

Declaration of Competing Interest

The authors declare that they have no known competing financial interests or personal relationships that could have appeared to influence the work reported in this paper.

Data availability

Data will be made available on request.

References

Allwood, J.M., Duncan, S.R., Cao, J., Groche, P., Hirt, G., Kinsey, B., Kuboki, T., Liewald, M., Sterzing, A., Tekkaya, A.E., 2016. Closed-loop control of product properties in metal forming. CIRP Ann. 65, 573–596. https://doi.org/10.1016/J.CIRP.2016.06.002.

Baral, M., Al-Jewad, A., Breunig, A., Groche, P., Ha, J., Korkolis, Y.P., Kinsey, B.L., 2022. Acoustic emission monitoring for necking in sheet metal forming. J. Mater. Process Technol. 310. https://doi.org/10.1016/J.JMATPROTEC.2022.117758.

Barlat, F., Brem, J.C., Yoon, J.W., Chung, K., Dick, R.E., Lege, D.J., Pourboghrat, F., Choi, S.H., Chu, E., 2003. Plane stress yield function for aluminum alloy sheets—part 1: theory. Int J. Plast. 19, 1297–1319. https://doi.org/10.1016/S0749-6419(02)00019-0.

Chen, K., Breunig, A., Ha, J., Kinsey, B.L., Groche, P., Korkolis, Y.P., 2022. Robustness of deep-drawing finite-element simulations to process variations. Int. J. Mater. Form. 15, 1–17. https://doi.org/10.1007/S12289-022-01695-3.

Chen, Z., Zhao, J., Fang, G., 2019. Finite element modeling for deep-drawing of aluminum alloy sheet 6014-T4 using anisotropic yield and non-AFR models. Int. J. Adv. Manuf. Technol. 104, 535–549. https://doi.org/10.1007/S00170-019-03921-W.

DIN EN ISO 10113:2021-06, Metallische Werkstoffe - Blech und Band - Bestimmung der senkrechten Anisotropie (ISO 10113:2020–11).

DIN EN ISO 12004–2:2021-07, Metallische Werkstoffe - Bestimmung der Grenzformänderungskurve für Bleche und Bänder - Teil 2: Bestimmung von Grenzformänderungskurven im Labor (ISO 12004–2:2021–07).

DIN EN ISO 16808:2021-12, Metallische Werkstoffe - Blech und Band - Bestimmung der biaxialen Spannung/Dehnung-Kurve durch einen hydraulischen Tiefungsversuch mit optischen Messsystemen (ISO/FDIS 16808:2021–12).

DIN EN ISO 6892–1:2020-06, Metallische Werkstoffe - Zugversuch - Teil 1: Prüfverfahren bei Raumtemperatur (ISO 6892–1:2019).

Doege, E., Seidel, H.J., Griesbach, B., Yun, J.W., 2002. Contactless on-line measurement of material flow for closed loop control of deep drawing. J. Mater. Process Technol. 130–131, 95–99. https://doi.org/10.1016/S0924-0136(02)00763-X.

Endelt, B., Tommerup, S., Danckert, J., 2013. A novel feedback control sySTEM – CONTRolling the material flow in deep drawing using distributed blank-holder force. J. Mater. Process. Technol. 213, 36–50. https://doi.org/10.1016/J.JMATPROTEC.2012.08.003.

Griesbach, B., 2000. In-Prozeß Stoffflußmessung zur Analyse und Führung von Tiefziehvorgängen. Zugl.: Hannover, Univ., Diss., 1999, Düsseldorf.

Gu, M., Eisenstat, S.C., 1996. Efficient Algorithms for Computing a Strong Rank-Revealing QR Factorization. https://doi.org/10.1137/0917055 17, 848–869. https://doi.org/10.1137/0917055.

Guo, Y.Q., Batoz, J.L., Naceur, H., Bouabdallah, S., Mercier, F., Barlet, O., 2000. Recent developments on the analysis and optimum design of sheet metal forming parts using a simplified inverse approach. Comput. Struct. 78, 133–148. https://doi.org/10.1016/S0045-7949(00)00095-X.

Harsch, D., Heingärtner, J., Renkci, Y., Hora, P., 2017. Influence of scattering material properties on the robustness of deep drawing processes. Model Based Control for Smart Forming Processes: 10th Forming Technology Forum.

Heingärtner, J., 2012. Intelligente Datenanalyse für die zerstörungsfreie Werkstoffprüfung in der Umformtechnik. https://doi.org/10.3929/ETHZ-A-007317840.

Herman, J., Usher, W., 2017. SALib: an open-source python library for sensitivity analysis. J. Open Source Softw. 2, 97. https://doi.org/10.21105/JOSS.00097.

Herrmann, J., Merklein, M., 2018. Improvement of deep drawability of ultra-fine grained 6000 series aluminum alloy by tailored heat treatment. Procedia Manuf. 15, 976–983. https://doi.org/10.1016/J.PROMFG.2018.07.397.

Herrmann, J., 2020. Kumulatives Walzplattieren: Bewertung der Umformeigenschaften mehrlagiger Blechwerkstoffe der ausscheidungshärtbaren Legierung AA6014. https://doi.org/10.25593/978–3-96147–345-8.

Hippke, H., Berisha, B., Hora, P., 2020. A full-field optimization approach for iterative definition of yielding for non-quadratic and free shape yield models in plane strain. IOP Conf. Ser. Mater. Sci. Eng. 967, 012084 https://doi.org/10.1088/1757-899X/967/1/012084.

Hockett, J.E., Sherby, O.D., 1975. Large strain deformation of polycrystalline metals at low homologous temperatures. J. Mech. Phys. Solids 23, 87–98. https://doi.org/10.1016/0022-5096(75)90018-6.

Huang, C., Radi, B., Hami, A. el, 2016. Uncertainty analysis of deep drawing using surrogate model based probabilistic method. Int. J. Adv. Manuf. Technol. 2016 86:9 86 3229–3240. https://doi.org/10.1007/S00170-016-8436-4.

Kott, M., Kraft, M., Emrich, A., Groche, P., 2021. Variance based sensitivity analysis of deep drawing processes based on neural networks using Sobol indices. IOP Conf. Ser. Mater. Sci. Eng. 1157, 012089 https://doi.org/10.1088/1757-899X/1157/1/012089.

Lim, Y., Venugopal, R., Ulsoy, A.G., 2008. Advances in the control of sheet metal forming. IFAC Proc. Vol. 41, 1875–1883. https://doi.org/10.3182/20080706-5-KR-1001.00320.

Maier, S., Schmerbeck, T., Liebig, A., Kautz, T., Volk, W., 2017. Potentials for the use of tool-integrated in-line data acquisition systems in press shops. J. Phys. Conf. Ser. 896, 012033 https://doi.org/10.1088/1742-6596/896/1/012033.

McKay, M.D., Beckman, R.J., Conover, W.J., 1979. A comparison of three methods for selecting values of input variables in the analysis of output from a computer code. Technometrics 21, 239. https://doi.org/10.2307/1268522.

Mork, R., 2012. Qualitätsbewertung und-regelung für die Fertigung von Karosserieteilen in Presswerken auf Basis Neuronaler Netze. Herbert Utz Verl.

Neugebauer, R., Hoffmann, M., Roscher, H.-J., Scheffler, S., Wolf, K., 2006. Control of sheet-metal forming processes with piezoactuators in smart structures. Smart Structures and Materials 2006: Industrial and Commercial Applications of Smart Structures Technologies 6171, 61710E. https://doi.org/10.1117/12.657387.

Neuhauser, F.M., Struck, R., Mautz, H., Manopulo, N., Hora, P., 2019. Sensor placement design strategy and quality estimation in modern car body production using stochastic finite element methods. Procedia Manuf. 27, 104–111. https://doi.org/10.1016/J.PROMFG.2018.12.051.

Ostermann, F., 2014. Anwendungstechnologie aluminium. Anwend. Alum. https://doi.org/10.1007/978-3-662-43807-7.

Pedregosa, F., Michel, V., Grisel, O., Blondel, M., Prettenhofer, P., Weiss, R., Vanderplas, J., Cournapeau, D., Varoquaux, G., Gramfort, A., Thirion, B., Dubourg, V., Passos, A., Brucher, M., Perrot Matthieu, Duchesnay, F., 2011. Scikit-learn: machine learning in python. J. Mach. Learn. Res. 12, 2825–2830.

Pham, Q.T., Kim, Y.-S., 2022. Evaluation on flexibility of phenomenological hardening law for automotive sheet metals. Metals 2022 Vol. 12 (578), 578 12. https://doi.org/10.3390/MET12040578.

Polyblank, J.A., Allwood, J.M., Duncan, S.R., 2014. Closed-loop control of product properties in metal forming: a review and prospectus. J. Mater. Process Technol. 214, 2333–2348. https://doi.org/10.1016/J.JMATPROTEC.2014.04.014.

Ryser, M., Neuhauser, F.M., Hein, C., Hora, P., Bambach, M., 2021. Surrogate model–based inverse parameter estimation in deep drawing using automatic knowledge acquisition. Int. J. Adv. Manuf. Technol. 117, 997–1013. https://doi.org/10.1007/S00170-021-07642-X.

Saltelli, A., Ratto, M., Andres, T., Campolongo, F., Cariboni, J., Gatelli, D., Saisana, M., Tarantola, S., 2008. Global sensitivity analysis: The primer. Global Sensitivity Analysis: The Primer 1–292. https://doi.org/10.1002/9780470725184.

Sobol, I.M., 1993. Sensitivity estimates for nonlinear mathematical models. Math. Model. Comput. Exp. 1, 407–414.

Markus Strehlitz, 2015. Roboter sucht Beulen und Risse [WWW Document]. URL ⟨https://quality-engineering.industrie.de/branchen/metall-und-maschinenbau/roboter-sucht-beulen-und-risse/#slider-intro-1⟩ (accessed 11.17.22).

Swift, H.W., 1952. Plastic instability under plane stress. J. Mech. Phys. Solids 1, 1–18. https://doi.org/10.1016/0022-5096(52)90002-1.

Tommerup, S., Endelt, B., 2012. Experimental verification of a deep drawing tool system for adaptive blank holder pressure distribution. J. Mater. Process Technol. 212, 2529–2540. https://doi.org/10.1016/J.JMATPROTEC.2012.06.015.

Tschaetsch, H., 2006. Metal forming practise. Metal Forming Practise: Processes - Machines - Tools. Springer Berlin Heidelberg. https://doi.org/10.1007/3-540-33217-0.

Volk, W., Hora, P., 2011. New algorithm for a robust user-independent evaluation of beginning instability for the experimental FLC determination. Int. J. Mater. Form. 4, 339–346. https://doi.org/10.1007/S12289-010-1012-9.

Wang, C., Zhang, J.J., Goan, N., 2005. Draw-in map — a road map for simulation-guided die tryout and stamping process control. AIP Conf. Proc. 778, 66. https://doi.org/10.1063/1.2011195.

Zöller, F., Vera, S., Merklein, M., 2015. Experimental and numerical investigation on a pressure dependent friction model. Key Eng. Mater. 639, 403–410. https://doi.org/10.4028/WWW.SCIENTIFIC.NET/KEM.639.403.